

THE HST/ACS COMA CLUSTER SURVEY. II. DATA DESCRIPTION AND SOURCE CATALOGS¹

DEREK HAMMER^{2,3}, GIJS VERDOES KLEIJN⁴, CARLOS HOYOS⁵, MARK DEN BROK⁴, MARC BALCELLS^{6,7}, HENRY C. FERGUSON⁸, PAUL GOUDFROOIJ⁸, DAVID CARTER⁹, RAFAEL GUZMÁN¹⁰, REYNIER F. PELETIER⁴, RUSSELL J. SMITH¹¹, ALISTER W. GRAHAM¹², NEIL TRENTAM¹³, ERIC PENG^{14,15}, THOMAS H. PUZIA¹⁶, JOHN R. LUCEY¹¹, SHARDHA JOGEE¹⁷, ALFONSO L. AGUERRI⁶, DAN BATCHELDOR¹⁸, TERRY J. BRIDGES¹⁹, JONATHAN I. DAVIES²⁰, CARLOS DEL BURGO^{21,22}, PETER ERWIN^{23,24}, ANN HORNSCHMEIER³, MICHAEL J. HUDSON²⁵, AVON HUXOR²⁶, LEIGH JENKINS³, ARNA KARICK⁹, HABIB KHOSROSHAHI²⁷, EHSAN KOURKCHI²⁷, YUTAKA KOMIYAMA²⁸, JENNIFER LOTZ²⁹, RONALD O. MARZKE³⁰, IRINA MARINOVA¹⁷, ANA MATKOVIC⁸, DAVID MERRITT¹⁸, BRYAN W. MILLER³¹, NEAL A. MILLER^{32,33}, BAHAM MOBASHER³⁴, MUSTAPHA MOUHCINE⁹, SADANORI OKAMURA³⁵, SUE PERCIVAL⁹, STEVEN PHILLIPPS²⁵, BIANCA M. POGGIANTI³⁶, RAY M. SHARPLES¹¹, R. BRENT TULLY³⁷, EDWIN VALENTIJN⁴

Draft version March 23, 2010

ABSTRACT

The Coma cluster, Abell 1656, was the target of a HST-ACS Treasury program designed for deep imaging in the F475W and F814W passbands. Although our survey was interrupted by the ACS instrument failure in early 2007, the partially-completed survey still covers $\sim 50\%$ of the core high-density region in Coma. Observations were performed for twenty-five fields with a total coverage area of 274 arcmin², and extend over a wide range of cluster-centric radii (~ 1.75 Mpc or 1 deg). The majority of the fields are located near the core region of Coma (19/25 pointings) with six additional fields in the south-west region of the cluster. In this paper we present SEXTRACTOR source catalogs generated from the processed images, including a detailed description of the methodology used for object detection and photometry, the subtraction of bright galaxies to measure faint underlying objects, and the use of simulations to assess the photometric accuracy and completeness of our catalogs. We also use simulations to perform aperture corrections for the SEXTRACTOR Kron magnitudes based only on the measured source flux and its half-light radius. We have performed photometry for $\sim 76,000$ objects that consist of roughly equal numbers of extended galaxies and unresolved objects. Approximately two-thirds of all detections are brighter than $F814W = 26.5$ mag (AB), which corresponds to the 10σ point-source detection limit. We estimate that Coma members are 5-10% of the source detections, including a large population of compact objects (primarily GCs, but also cEs and UCDs), and a wide variety of extended galaxies from cD galaxies to dwarf low surface brightness galaxies. The initial data release for the HST-ACS Coma Treasury program was made available to the public in August 2008. The images and catalogs described in this study relate to our second data release.

Subject headings: galaxies: clusters – instrument: HST: ACS

¹ Based on observations with the NASA/ESA *Hubble Space Telescope* obtained at the Space Telescope Science Institute, which is operated by the association of Universities for Research in Astronomy, Inc., under NASA contract NAS 5-26555. These observations are associated with program GO10861.

² Department of Physics and Astronomy, Johns Hopkins University, 3400 North Charles Street, Baltimore, MD 21218, USA.

³ Laboratory for X-Ray Astrophysics, NASA Goddard Space Flight Center, Code 662.0, Greenbelt, MD 20771, USA.

⁴ Kapteyn Astronomical Institute, University of Groningen, PO Box 800, 9700 AV Groningen, The Netherlands.

⁵ School of Physics and Astronomy, The University of Nottingham, University Park, Nottingham, NG7 2RD, UK.

⁶ Instituto de Astrofísica de Canarias, 38200 La Laguna, Tenerife, Spain.

⁷ Isaac Newton Group of Telescopes, Apartado 321, 38700 Santa Cruz de La Palma, Spain.

⁸ Space Telescope Science Institute, 3700 San Martin Drive, Baltimore, MD 21218, USA.

⁹ Astrophysics Research Institute, Liverpool John Moores University, Twelve Quays House, Egerton Wharf, Birkenhead CH41 1LD, UK.

¹⁰ Department of Astronomy, University of Florida, PO Box 112055, Gainesville, FL 32611, USA.

¹¹ Department of Physics, University of Durham, South Road, Durham DH1 3LE, UK.

¹² Centre for Astrophysics and Supercomputing, Swinburne University of Technology, Hawthorn, VIC 3122, Australia.

¹³ Institute of Astronomy, Madingley Road, Cambridge CB3 0HA, UK.

¹⁴ Department of Astronomy, Peking University, Beijing 100871,

China.

¹⁵ Kavli Institute for Astronomy and Astrophysics, Peking University, Beijing 100871, China.

¹⁶ Plaskett Fellow, Herzberg Institute of Astrophysics, National Research Council of Canada, 5071 West Saanich Road, Victoria, BC V9E 2E7, Canada.

¹⁷ Department of Astronomy, University of Texas at Austin, 1 University Station C1400, Austin, TX 78712, USA.

¹⁸ Department of Physics, Rochester Institute of Technology, 85 Lomb Memorial Drive, Rochester, NY 14623, USA.

¹⁹ Department of Physics, Engineering Physics and Astronomy, Queen's University, Kingston, Ontario K7L 3N6, Canada.

²⁰ School of Physics and Astronomy, Cardiff University, The Parade, Cardiff CF24 3YB, UK.

²¹ UNINOVA-CA3, Campus da Caparica, Quinta da Torre, Monte de Caparica 2825-149, Caparica, Portugal.

²² School of Cosmic Physics, Dublin Institute for Advanced Studies, Dublin 2., Ireland.

²³ Max-Planck-Institut für Extraterrestrische Physik, Giessenbachstrasse, D-85748 Garching, Germany.

²⁴ Universitätssternwarte, Scheinerstrasse 1, 81679 München, Germany.

²⁵ Department of Physics and Astronomy, University of Waterloo, 200 University Avenue West, Waterloo, Ontario N2L 3G1, Canada.

²⁶ Astrophysics Group, H. H. Wills Physics Laboratory, University of Bristol, Tyndall Avenue, Bristol BS8 1TL, UK.

²⁷ School of Astronomy, Institute for Research in Fundamental Sciences (IPM), P.O. Box 19395-5531, Tehran, Iran.

²⁸ Subaru Telescope, National Astronomical Observatory of

1. INTRODUCTION

The Coma cluster has been the subject of numerous surveys from X-ray to radio owing to its richness, proximity ($z \sim 0.023$), and accessibility at high Galactic latitude ($b \sim 88$ deg). Coma member galaxies have been critical to our understanding of galaxy formation and evolution in dense environments, and provide a local benchmark for comparative studies of galaxy evolution in different environments and at higher redshift (e.g. the morphology-density relation and the Butcher-Oemler effect; Dressler 1980; Butcher & Oemler 1984). However, the properties of intrinsically faint objects in the Coma cluster are not yet well characterized compared to other local clusters such as Virgo and Fornax. The resolution and sensitivity afforded by the *Hubble Space Telescope-Advanced Camera for Surveys* (HST-ACS; Ford et al. 1998) has allowed for detailed studies of faint and compact systems in Coma (Carter et al. 2008, hereafter Paper I), such as measuring the structural parameters of dwarf galaxies (Hoyos et al. 2010, *in prep*, hereafter Paper III), constraining the globular cluster population (Peng et al. 2010, *submitted*, hereafter Paper IV), studying the nature of compact elliptical galaxies (Price et al. 2009, hereafter Paper V) and ultra-compact dwarf galaxies (UCDs), and establishing membership for faint cluster member galaxies by morphology.

The ACS Coma Cluster Treasury survey was initiated in HST Cycle 15 following the success of the ACS cluster surveys performed in Virgo (Côté et al. 2004) and Fornax (Jordán et al. 2007). In contrast to the Virgo and Fornax surveys that targeted individual early-type galaxies, the Coma fields were arranged to maximize spatial coverage at the cluster core as well as provide targeted observations at an off-center region of Coma. The advantage of this observing strategy is that it allows for *statistical* measurements of faint cluster members (e.g. the luminosity function; Trentham et al. 2010, *in prep*, hereafter Paper VI) while also probing the effects of the cluster environment across a wide range of cluster-centric distance. Although the Coma cluster is located at a distance of 100 Mpc (5-6 times more distant than Virgo and Fornax), the spatial resolution afforded by HST-ACS is similar to current ground-based observations of Virgo and Fornax (~ 50 pc).

The ACS Coma Cluster Treasury survey was awarded

164 orbits (82 fields), although the survey was only 28% complete when interrupted by the ACS failure in early 2007. A description of the observing program and image reductions is provided in Paper I. In this paper, the second in the series, we present SEXTRACTOR catalogs for our ACS observations. The catalogs include astrometric and photometric data for $\sim 76,000$ source detections, as well as basic object classifications (i.e. extended galaxy or point source). The majority of detections are background galaxies, although we detect several thousand globular clusters (GCs) and several hundred galaxies that are likely members of the Coma cluster. The SEXTRACTOR catalogs are optimized for detection of unresolved sources including the large GC population. The catalogs do not provide an exhaustive list of extended galaxies in Coma, especially for the faintest low surface brightness (LSB) galaxies, for which visual inspection of the images is more successful than automated detection.

This paper is organized as follows: imaging data and calibrations in Section 2, the methodology for creating source catalogs, including a treatment of bright galaxies in Section 3, and simulations to estimate the completeness and photometric accuracy of the source catalogs in Section 4. As described in Paper I, we assume that the Coma cluster is located at a distance of 100 Mpc ($z = 0.023$), which corresponds to a distance modulus of 35 mag and angular scale of 0.463 kpc arcsec $^{-1}$ for $H_0 = 71$ km s $^{-1}$ Mpc $^{-1}$, $\Omega_\Lambda = 0.73$, and $\Omega_M = 0.27$.

2. DATA

We refer the reader to Paper I for a detailed description of the observing strategy, science objectives, and the image pipeline for the HST-ACS Coma Cluster Treasury Survey. Here we provide only a brief summary of the survey. The ACS Wide Field Camera, with a field of view of 11.3 arcmin 2 , imaged the Coma cluster in 25 fields with the F475W and F814W filters. The ACS observation footprint is shown relative to the virial radius of the Coma cluster in Figure 1 ($r_{\text{vir}} = 2.9$ Mpc or 1.7 deg; Lokas & Mamon 2003). The majority of the survey fields (19 of 25) are located within 0.5 Mpc (0.3 deg) of the center of Coma³⁸, mainly covering the regions around the two central galaxies NGC 4874 and NGC 4889 (although NGC 4889 was not observed). Six additional fields are located between 0.9 - 1.75 Mpc (0.5 - 1.0 deg) south-west of the cluster center. The core and south-west regions of the Coma cluster are sometimes referred to as ‘Coma-1’ and ‘Coma-3’, respectively (Komiyama et al. 2002).

Processed images and initial source catalogs for the ACS Coma Cluster Treasury program were released in August 2008 (Data Release 1)³⁹. This paper describes the images and source catalogs provided in Data Release 2 (DR2), which includes several enhancements to the initial release such as: (a) improvement of the relative alignment between F814W and F475W images and thus aperture-matched color information, (b) refinement of the image astrometry, (c) application of aperture corrections to the SEXTRACTOR photometry, and (d) subtraction of bright galaxies to recover faint underlying objects.

³⁸ The center of the Coma cluster is taken as the location of the central cD galaxy, NGC 4874 ($\alpha = 194^\circ.89874$ and $\delta = 27^\circ.95927$).

³⁹ Available from MAST (archive.stsci.edu/prepds/coma/) and Astro-WISE (www.astro-wise.org/projects/COMALS/).

Japan, 650 North A’ohoku Place, Hilo, HI 96720, USA.

²⁹ Leo Goldberg Fellow, National Optical Astronomy Observatory, 950 North Cherry Avenue, Tucson, AZ 85719, USA.

³⁰ Department of Physics and Astronomy, San Francisco State University, San Francisco, CA 94132-4163, USA.

³¹ Gemini Observatory, Casilla 603, La Serena, Chile.

³² Department of Astronomy, University of Maryland, College Park, MD, 20742-2421, USA

³³ Jansky Fellow of the National Radio Astronomy Observatory. The National Radio Astronomy Observatory is a facility of the National Science Foundation operated under cooperative agreement by Associated Universities, Inc.

³⁴ Department of Physics and Astronomy, University of California, Riverside, CA, 92521, USA

³⁵ Department of Astronomy, University of Tokyo, 7-3-1 Hongo, Bunkyo, Tokyo 113-0033, Japan.

³⁶ INAF-Osservatorio Astronomico di Padova, Vicolo dell’Osservatorio 5, Padova I-35122, Italy.

³⁷ Institute for Astronomy, University of Hawaii, 2680 Woodlawn Drive, Honolulu, HI 96822, USA.

2.1. Drizzled Images

The nominal observing sequence for each field consists of four dither positions ('DITHER-LINE' pattern type) each having an exposure time of 350 s and 640 s for the F814W and F475W filters, respectively. Only two dither positions are available across the ACS inter-CCD chip gap resulting in a degraded 3'' band that runs horizontally across the center of every image. Four fields were observed with less than four dither positions due to the failure of the ACS instrument while the sequence was partially complete. In Table 1 we list the details for each field including a unique identifier given by the HST visit number, coordinates, image orientation, number of dithers, and the integrated exposure time in each band.

The dithered exposures were individually dark- and bias-subtracted, and flat-fielded through the standard HST-CALACS pipeline software. The MultiDrizzle software (Koekemoer et al. 2002) was used to combine the dither positions and create a final image. The steps in the MultiDrizzle process include (a) aligning the dithered exposures, (b) identifying cosmic rays using a median filter and 'cleaning', (c) weighting pixels from the individual dithers by the inverse variance of the background/instrumental noise, and (d) mapping the weighted exposures to an output grid with a pixel size of 0''.05 ($\text{pixfrac}=0.8$ and $\text{scale}=1.0$).

The identification of cosmic rays by the MultiDrizzle software was inefficient in regions of the image not covered by the full dither pattern. The *lacosmic* routine (van Dokkum 2001) was therefore used to assist with cosmic ray identification within the ACS chip gap and also across the full image for fields with less than four dither positions. A side effect of the *lacosmic* routine is that pixels associated with extreme surface brightness gradients in the image may be erroneously assigned large (negative or positive) values. Although this affects only a small number of pixels, we have corrected these pixels in the DR2 images by replacing their values with the local median. Owing to erratic behavior, we do not apply *lacosmic* to regions at the image edge not covered by the full dither pattern, thus the majority of remaining cosmic rays found in DR2 images are located in these regions.

2.2. Relative Astrometry

A slight spatial offset between F475W and F814W images (~ 0.3 pixels) was discovered soon after the initial data release. This offset has a non-negligible effect on the aperture-matched color measurements of unresolved or marginally resolved objects. Images were realigned by measuring the residual shift between the F475W and F814W frames using compact sources as a reference, and then re-drizzling the F475W band to match the original F814W image. For three fields (visits 3, 10, and 59), it was necessary to re-drizzle the images in both filters to a common pixel position. In Figure 2 we show the spatial offsets between F475W and F814W images after performing the realignment procedure. The DR2 images are aligned to within ~ 0.05 pixels along each axis.

2.3. Absolute Astrometry

A two-step process was used to calculate the astrometry for each ACS image, starting with the solution calculated by MultiDrizzle and then performing a fine adjustment using the SCAMP software (v1.4; Bertin 2006). The

initial spatial registration of images was calculated with MultiDrizzle using reference stars in the HST Guide Star Catalog. Astrometry solutions were reliable to only $\sim 1''$ (1σ rms offset, as compared to the SDSS coordinate system), owing to the dearth of reference stars in the Coma fields, which are located at high Galactic latitude ($b \sim 88$ deg).

Second pass solutions for the image astrometry were performed using SCAMP with the goal of aligning ACS images to the Sloan Digital Sky Survey (SDSS) coordinate system. Both stars and galaxies from SDSS DR6 were selected as reference objects, which increased the ACS and SDSS matched sample to 18-36 objects for each field. We excluded saturated stars, ACS objects that were blended with nearby sources, or objects located in regions of the ACS image with reduced exposure time. Astrometry solutions were calculated for each field using a range of values for the SCAMP input parameters CROSSID_RADIUS, ASTRCLIP_NSIGMA, and FWHM_THRESHOLDS. We forced SCAMP to solve the ACS astrometry *without* using higher order distortion terms (DISTORT_DEGREES = 1) as these values are well constrained by the HST-ACS pipeline (Meurer et al. 2003). We chose the SCAMP configuration that gave the 'best' reduced chi-squared fit (between $0.9 \lesssim \chi^2 \lesssim 1.2$) and the smallest final offset between ACS and SDSS reference objects. This procedure was performed in the F814W band and the final astrometry solutions were applied to images in both filters.

In Figure 3 we show the average offset in right ascension and declination for matched ACS/SDSS objects both before and after using SCAMP. The diagram shows that the final astrometry solutions for the ACS images are statistically consistent with the SDSS system. The rms spread is 0.1-0.2'' for each coordinate, which is consistent with the nominal precision of the SDSS astrometry for extended objects (Pier et al. 2003).

2.4. RMS Maps

RMS maps were created for every image that are used to establish the detection threshold for source identification and to derive photometric errors. The RMS maps were constructed from the inverse-variance maps produced by MultiDrizzle, which are stored in the [WHT] extension of the fits images. The WHT maps estimate the background and instrumental uncertainties related to the flat-field, dark current, read noise, and the effective exposure time across the image.

We must apply a correction to the RMS maps in order to derive accurate photometric errors. The single-pixel noise estimates cannot simply be summed in quadrature to derive error estimates for an extended region, because the Multidrizzle process introduces a correlation of the noise in neighboring pixels (see Fruchter & Hook 2002). Since we are interested in measuring the noise across objects that are larger than a few pixels, we must apply a scaling factor to the RMS map to recover its uncorrelated value over larger length scales (e.g. Casertano et al. 2000). The corrected RMS map is given by:

$$RMS = \frac{1}{\sqrt{WHT} \times f} \quad (1)$$

where f is the scalar correction for correlated noise, commonly referred to as the 'variance reduction factor'.

We have measured the variance reduction factor for a subset of our images by selecting a relatively empty 512x512 pixel region inside each image, then we perform the following steps: (a) normalization of the pixels by the effective exposure time, (b) masking of real objects identified using a median filter, (c) measurement and subtraction of the background, and (d) photometry on its autocorrelation image in order to measure the peak pixel flux relative to the total flux, e.g. the correlation factor is $f = \text{peak}/\text{total}$, where a value of 1 indicates that the image is uncorrelated at any pixel scale. We have measured the correction factor for a subset of images in both filters, recovering an average value of $f = 0.77 \pm 0.08$ (1σ rms). The average value is applied to all WHT maps as the correction factor depends primarily on the choice of MultiDrizzle parameters *pixfrac* and *scale* (which are constants in our image pipeline).

2.5. Flag Maps

Flag maps were created for every image in order to identify pixels with low effective exposure time. The effective exposure time varies abruptly across each image owing to regions that are only partially covered by the dither pattern. These regions include the ACS chip gap and the image border, which cover 5-10% of the total image area. We have added additional flags to identify pixels that may be affected by very bright galaxies (described in §5) and for pixels in close proximity to the image edge. We have assigned a single binary-coded flag value to each pixel that indicate the following: [1] associated with a bright galaxy, [2] located within 32 pixels of the image edge, [4] an effective exposure time less than 2/3 the total integration time, and [8] zero effective exposure. The order was chosen such that higher flags correspond to regions of the image where object detection and photometry are more likely to have systematic effects.

The main purpose of the flag maps is to identify large regions of each image with similar completeness limits. We note that cosmic rays cleaned by MultiDrizzle often leave a few pixels with low effective exposure, but have little impact on the ability to detect underlying sources. To avoid flagging these pixels, we applied a 7-pixel median filter to the effective exposure map prior to imposing the low-exposure criteria. A few heavily-cleaned cosmic ray events remain flagged in each map.

3. SOURCE CATALOGS

The DR2 source catalogs were created using the SEXTRACTOR software (version 2.5; Bertin & Arnouts 1996). SEXTRACTOR was operated in ‘dual-image mode’ which uses separate images for detection and photometry. Dual-image mode allows for a straightforward consolidation of multi-band photometry into a single source catalog, and allows for aperture-matched color measurements. The F814W band was chosen as the detection image for both filters because it offers higher S/N for most sources, and results in less galaxy ‘shredding’ (i.e. a single source is deblended into multiple objects) as galaxy structure tends to be less ‘clumpy’ in F814W as compared to the F475W band. Object detection was performed on a convolved version of the detection image (gaussian kernel of FWHM=2.5 pixels) to limit the number of spurious detections. We used the background RMS

maps (§2.4) to weight the detection threshold across the convolved image, which allows for more reliable detections at faint magnitudes.

SEXTRACTOR performs source detection using a ‘connected pixel’ algorithm, i.e. a detection is registered when a specified number of contiguous pixels satisfies the detection threshold (set by the DETECT_MINAREA and DETECT_THRESH parameters). It then performs a second pass analysis of source detections to identify and deblend objects that are connected on the sky (set primarily by the DEBLEND_MINCONT and DEBLEND_NTHRESH parameters). Values for the detection and deblend parameters were chosen after testing a wide range of values and verifying by visual inspection that obvious sources were detected while minimizing the number of spurious detections. The full set of SEXTRACTOR parameters used for this study is presented in the Appendix. Finally, the detections were cross-referenced with the flag maps described in §2.5 and combined using the bitwise inclusive OR operation across pixels that satisfy the detection threshold. The resulting flag values are given by the IMAFLAGS_ISO field in the source catalogs, and the total number of flagged pixels is given by NIMAFLAGS_ISO.

SEXTRACTOR photometry was performed using a variety of apertures, such as (a) isophotal apertures which measure the flux only in pixels that satisfy the detection threshold (i.e. MAG_ISO magnitudes, which are recommended for color measurements), (b) adjustable elliptical apertures that are scaled according to the isophotal light profile (e.g. MAG_AUTO Kron apertures and MAG_PETRO Petrosian apertures), and (c) a set of nine fixed circular apertures with radii extending between 0''.06-6.0. Magnitudes are reported in the instrumental F475W and F814W AB magnitude system. We use magnitude zeropoints of 26.068 and 25.937 for the F475W and F814W bands, respectively, which were calculated separately for each visit (but resulting in identical zeropoints) following the procedure in the ACS Data Handbook (their Section 6.1.1). SEXTRACTOR estimates the photometric errors by adding in quadrature both the background/instrumental errors taken from the RMS maps and the Poisson errors for the measured source counts.

Source catalogs were created separately for each visit. The ACS fields in the central region of Coma have small overlap (see Figure 1), thus there are duplicate detections near the edges of these images. For the purpose of discussing properties of the total source population, we have concatenated source catalogs from the individual visits using a 0''.5 search radius to identify duplicate detections (0''.5 corresponds to the 3σ rms uncertainty of our image astrometry); for each match, we keep the source with a lower flag value to limit systematic effects (see §2.5), else we keep the source with the highest S/N. After removing duplicate detections, the catalog consists of $\sim 76,000$ unique source detections, with a magnitude distribution as shown in Figure 4. The raw number counts peak at $F814W \approx 27$ and $F475W \approx 27.5$ mag, and fall off rapidly at fainter magnitudes. The average signal-to-noise (S/N) ratio for the SEXTRACTOR detections is provided in Figure 5, shown as contours on a magnitude-size diagram. Object size is taken as the SEXTRACTOR half-light radius in the F814W band (FLUX_RADIUS_3), which is the size of the circular aperture that encloses 50% of the flux in the Kron aperture. From the diagram, the 10σ point-source

detection limit is $F814W=26.5$ mag. The S/N spans a wide range at a given magnitude owing to the variety of sources detected in the Coma cluster and the background; the majority of detections are background galaxies, while $\sim 5\%$ of objects are located inside the Coma cluster. In the next section we address objects that were not detected owing to their proximity to bright cluster member galaxies.

3.1. Bright Galaxy Subtraction

We have subtracted the light distribution from bright galaxies in DR2 images in order to improve object detection and photometry for faint underlying sources (e.g. dwarf galaxies, GCs). The candidates for light subtraction are the 31 galaxies that have magnitudes brighter than $F814W=15.0$. We modeled the light distribution using the software package GALPHOT (Franx et al. 1989) within the Astro-WISE system (Valentijn et al. 2007). GALPHOT allows for elliptical and higher-order isophotal light models that were fit to image cutouts of the bright galaxy sample. Objects located inside the light distribution of the target galaxy were masked prior to performing our fitting procedure. We selected the optimal light model by visual inspection of the residual images, and truncated the best-fitting model at the location where it is indistinguishable from the background noise. The best-fit light model was subtracted and the cutout was inserted back into the original image. We could not obtain a satisfactory solution for three bright galaxy candidates: one spiral galaxy was too irregular to be modeled with elliptical isophotes, and the other two galaxies were overlapping thus preventing a good solution. Basic properties of the remaining 28 galaxies are listed in Table 3.

In order to perform reliable source detection within regions of galaxy subtraction, we have corrected the RMS maps to account for photon noise from the bright galaxy and fitting errors. Specifically, we added the following term σ_{GSub}^2 to the variance map:

$$\sigma_{\text{GSub}}^2 = 1.05 \times \sigma_{\text{poisson}}^2, \quad (2)$$

where σ_{poisson} is the Poisson noise taken from the light distribution model, and we have added an additional 5% error to account for an imperfect fit (e.g. Del Burgo et al. 2008). We ran SEXTRACTOR on the galaxy-subtracted images (weighted by the updated RMS maps) using a configuration that is otherwise identical to that used for the original images.

New source detections were merged with the original source catalog using the following procedure. We defined a circular annulus for each subtracted galaxy with an inner and outer radius (r_{min} , r_{max}) as listed in Table 3. Within the inner radius large systematic residuals prevent the reliable detection of sources. The outer radius is defined in order to reject spurious detections located at the boundary of the truncated galaxy model. At locations beyond the outer radius, we retain the original measurements as the original and galaxy-subtracted catalogs include virtually the same real sources, as expected. We added to our final source catalog all sources from the galaxy-subtracted catalog that are located in the annulus. We also adopted values from the galaxy-subtracted catalog for duplicate detections in the annulus, which were identified using a $0''.5$ search radius. Figure 6 shows

one example image after performing galaxy subtraction, including the location of original and new source detections. As a result of subtracting bright galaxies, we have recovered 3291 additional sources that were detected out to $200''$ from the centers of the bright galaxies.

3.2. Objects in the Coma Cluster

Our source catalogs include both globular clusters and galaxies that are located inside the Coma cluster. GCs are the majority of cluster members, as several thousand are detected at magnitudes fainter than $F814W \approx 24$ (Paper IV). GCs are unresolved at the distance of Coma, thus their detection efficiency is relatively higher at faint magnitudes as compared to cluster member galaxies; we also fine-tuned the SEXTRACTOR configuration in order to optimize detection of the dominant GC population. We estimate that our catalogs also include a few hundred galaxies in the Coma cluster based on a list of morphology-selected candidates assembled by team members Harry Ferguson and Neal Trentham. The Coma member galaxies span a wide-range of morphology, including a cD galaxy (NGC 4874), barred disk galaxies (Marinova et al. 2010), compact elliptical galaxies (cE; Price et al. 2009), dwarf early-type galaxies (dE; nucleated and non-nucleated), dwarf irregular (dIrr) and spiral galaxies, and ultra-compact dwarf galaxies (UCD).

SEXTRACTOR, however, performs poorly for objects with low surface brightness, and hence our catalogs are not exhaustive for the cluster dwarf galaxy population. Based on visual inspection of the images, the SEXTRACTOR photometry is adequate for the majority of dwarf LSB galaxies with properties resembling typical cluster dwarf galaxies (i.e. dE and dIrr galaxies). The exception is for dwarf LSB galaxies located near relatively bright objects, for which SEXTRACTOR tends to shred the LSB galaxy into multiple objects, or does not register a detection. We have mitigated the fraction of shredded/missing dwarf LSB galaxies by subtracting the light distribution of the 28 brightest cluster member galaxies (§3.1).

SEXTRACTOR detection is far worse for a subset of dwarf LSB galaxies that appear as amorphous structures just visible above the background noise. The detection of such galaxies is poor regardless of their proximity to other objects. We refer to these galaxies as very low surface brightness galaxies (VLSBs; classified based on visual inspection), which is meant only for easy reference throughout this discussion, and is not an attempt at defining a new class of galaxy with a quantitative definition. We have identified ~ 50 VLSB galaxies that are likely Coma members owing to their preferred location in the central cluster region. Despite extensive tests using different SEXTRACTOR detection techniques (e.g. different detection/deblending parameters, convolution kernels, and also trying co-added and binned images), we found that SEXTRACTOR did not draw suitable apertures for the majority of VLSBs, or they were not detected. If a detection was registered, the VLSB galaxies were typically shredded into several objects, or were blended with nearby objects. In Figure 7, we show the SEXTRACTOR apertures associated with two VLSB galaxies that demonstrate these issues. We will address the nature of these galaxies and their photometry in a future paper.

3.3. Object Classification

In the following section we present an initial attempt to classify objects, real or otherwise, in the DR2 source catalogs. Object classifications are stored in the catalog `FLAGS_OBJ` parameter. A thorough description of these classifications is given below, and a summary of the flag values is also provided in the Appendix. We also discuss spurious sources in our catalogs owing to inaccurate galaxy separation and the chance alignment of random noise.

3.3.1. Extended Galaxies and Point Sources

The `SEXTRACTOR CLASS_STAR` parameter is a dimensionless value that classifies objects as extended or point-like based on a neural network analysis that compares the object scale and the image PSF. The parameter varies between 0-1, such that extended objects have values near 0 and point-like objects are closer to 1; less reliable classifications are assigned mid-range values. The galaxy/point source classification is improved by also considering the 50% light radius measured in the $F814W$ band. Specifically, we classify as galaxies those objects with `CLASS_STAR` < 0.5 and `FLUX_RADIUS_3` > 2.5 pixels (2.5 pix = 0".125, or 61 pc at the distance of Coma). These objects are assigned `FLAGS_OBJ` = 0. Objects that do not meet this criteria are considered point sources and are assigned `FLAGS_OBJ` = 1. From visual inspection we estimate that this classification scheme is ~95% reliable for objects brighter than $F814W$ = 24.0 mag. The `CLASS_STAR` parameter is not reliable at fainter magnitudes, we therefore rely on the 50% light radius criteria to classify the fainter objects. For the total catalog, there are roughly an equal number of sources classified as extended or point source.

In Figure 8, we have plotted our catalog sources in a magnitude-size diagram separated as extended galaxies and point sources. Our classification scheme clearly separates extended galaxies and intrinsically compact sources at magnitudes brighter than $F814W \approx 25$; at fainter magnitudes, the point source class includes an increasing population of unresolved galaxies. This can be seen more clearly from the magnitude histogram for extended galaxies and point sources shown in Figure 4. The extended galaxy population flattens at $F814W$ = 25 mag, or ~1-1.5 mag brighter than the total source population, owing to a higher fraction of unresolved galaxies. The diagram also shows that the point source population increases at magnitudes fainter $F814W$ = 22.5, which may initially reflect the UCD population in the Coma cluster (Chiboucas et al. 2010, *in prep*), and then the large number of GCs in the cluster at $F814W \gtrsim 24$ mag (Paper IV).

3.3.2. Cosmic Rays

Although the majority of cosmic rays were removed during assembly of the final images, a fraction of them remain in our catalogs, especially in areas not covered by the full dither pattern. Cosmic rays typically appear as compact detections that are bright in the $F814W$ image but with no counterpart in the $F475W$ band. As such, we found that cosmic rays may be identified by selecting candidates with characteristic sizes smaller than the ACS point-spread function (`FWHM_IMAGE` < 2.4 pixels), and then selecting objects with `MAG_ISO` colors redder

than $F475W - F814W = 3$. Since we perform source detection in the $F814W$ band alone, our catalogs are not well suited for identifying cosmic rays in the $F475W$ images.

Using the above criteria, we identified 18-619 cosmic ray candidates per ACS image at magnitudes brighter than $F814W$ = 26.5. We visually inspected the cosmic ray candidates and identified 2-10 real objects per image (primarily stars); the remaining cosmic ray candidates are flagged in our source catalogs (`FLAGS_OBJ` = 2). We found that cosmic rays are 12-25% of all detections in the border regions not covered by the full dither pattern, but are only ~1% of objects detected in other regions of the image; one notable exception is visit-12 where ~50% (6%) of objects are cosmic rays in these regions of the image, respectively.

3.3.3. Image Artifacts

We have visually identified a small number of detections in our source catalogs that correspond to image anomalies such as diffraction spikes and ‘ghost’ images from bright stars. For instance, a diffraction spike extends horizontally across the entire image for visit-13 due to a bright star located just outside the field of view. We have flagged detections that are a direct consequence of image artifacts or real sources whose photometry may be significantly affected by these features (`FLAGS_OBJ` = 3).

3.3.4. Galaxy Separation

We chose values for the `SEXTRACTOR` deblending parameters that minimize the fraction of shredded galaxies, and also result in roughly the same number of shredded objects as false blended objects for faint field galaxies in ACS images (e.g. ~5-10% of detections across $F814W$ = 23-27 mag are affected by object shredding or blending; Benítez et al. 2004). The balance between shredded and blended objects does not apply to the regions near bright extended galaxies in the Coma cluster, which tend to include more galaxy shreds; this is especially the case inside the extended halos of the bright early-type galaxies, where we observe the largest fraction of galaxy shreds. Such galaxy shreds have little impact on the photometry of the much brighter parent galaxy but result in spurious detections in our catalogs. We have limited the number of these spurious detections by subtracting the light distribution of the 28 brightest galaxies. This procedure, however, did not remove all galaxy shreds associated with the bright galaxy sample, and many examples remain in our catalogs near galaxies with intermediate magnitudes.

3.3.5. Random Noise

Spurious detections may result from the chance alignment of random noise fluctuations. We have estimated the fraction of such detections by running `SEXTRACTOR` on inverted images, which should give a reasonable estimate provided that the noise is symmetrical. This analysis applies to empty regions of the image, as it was necessary to mask objects in our catalog prior to running `SEXTRACTOR` on the inverted image. We found that $\lesssim 1\%$ of detections brighter than $F814W$ = 27.0 mag result from random noise, with a rapid increase at fainter magnitudes, which was verified for each image. The exceptions

are regions not covered by the full dither pattern for images with fewer than 4-dither positions (e.g. visits 3,12,13,14); in these cases, $\gtrsim 10\%$ of detections are random noise at magnitudes fainter than $F814W=25.0$.

4. SIMULATIONS

We have tested the reliability of the SEXTRACTOR photometry and assessed the completeness limits of our source catalog by injecting synthetic sources onto the ACS images and re-running our photometry pipeline. Specifically, we used the GALFIT software (Peng et al. 2002) to generate a suite of synthetic Sérsic models that uniformly span a large range in magnitude ($F814W=20-29$, $F475W=21-30$), effective radius ($R_{\text{eff}}=0.5-60$ pix), Sérsic index ($n_{\text{Ser}}=0.8-4.2$), and ellipticity ($e=0.0-0.8$). The models were convolved with a DrizzlyTim/TinyTim PSF (e.g. Krist 1993) truncated to 63×63 pixels to increase execution speed, and Poisson noise was added to match the noise characteristics of the data. For each ACS waveband, we randomly inserted a total of $\sim 200,000$ models across four fields that cover the cluster core and outskirts regions (visits 1,15,78, and 90), then SEXTRACTOR was run in a configuration identical to our pipeline as described in §2. The artificial sources were considered detected if SEXTRACTOR found a source within 4 pixels (~ 2 PSF FWHM) of the known position.

In this section, we describe the results of our simulations as it relates to detection efficiency and catalog depth (§4.1), and the missing-light problem associated with SEXTRACTOR photometry and our solution (§4.2).

4.1. Detection Efficiency

It is well known that the SEXTRACTOR detection efficiency is a function of object size and magnitude (e.g. Bershadsky et al. 1998; Cristóbal et al. 2003; Eliche-Moral et al. 2006). As such, we have measured the detection efficiency separately for models with similar size and magnitude, as well as Sérsic index and ellipticity, and discuss how the detection efficiency depends on these parameters.

Figure 10 shows the detection efficiency versus magnitude for our models. We have separated the models into four subsets based on Sérsic index and ellipticity, which throughout this section are referred to as models FC, FE, PC, and PE: flat (F) and peak (P) models have Sérsic indices that are smaller/larger than $n_{\text{Ser}}=2.25$, respectively; circular (C) and elliptical (E) models have ellipticities smaller/larger than $e=0.4$, respectively. The panels in Figure 10 show the detection efficiency for each model subset, which we further separate into six equally-spaced bins in logarithmic effective radius that span the range $R_{\text{eff}}=0.5-60$ pixels. The left-most curves in each panel trace the largest R_{eff} , which for a given magnitude represent galaxies with the lowest surface brightness. All efficiency curves show the same pattern: at the bright end efficiencies are near 100%, and then fall to zero with a similar slope. None of the curves reaches 100% efficiency (maximum rates are $\sim 96-98\%$) owing to artificial sources that were injected near relatively brighter galaxies. We note that our SEXTRACTOR catalogs reach 100% efficiency for moderately bright objects upon subtracting the brightest 28 galaxies from our images prior to source detection (§3.1). For a given magnitude, the detection efficiency depends primarily on object size (small R_{eff} gives

higher efficiency), followed by Sérsic index (models with large n_{Ser} have higher efficiencies), and to lesser extent on the ellipticity (high-ellipticity models have slightly higher detection rates), i.e. the detection efficiency is positively correlated with any model parameter that increases the central surface brightness.

In Table 2 we list the expected 80% completeness limits for our SEXTRACTOR catalogs based on our simulations. The completeness limits are given for the four model subgroups (FC, FE, PC, and PE) separated into the six logarithmically-spaced bins in R_{eff} ($F814W$ results are shown in Cols 2-7, and $F475W$ in Cols 8-13). The 80% completeness limits for point sources occurs at $F814W=26.8$ and $F475W=27.8$ mag for images with the nominal four dither positions; the $F814W$ limit is consistent with the magnitude distribution of our SEXTRACTOR catalogs presented in Figure 4.

4.2. Corrections to SEExtractor Kron Photometry

Next we have tested the accuracy of the SEXTRACTOR photometry by comparing its flux measurements to the magnitudes of the artificial objects. The SEXTRACTOR Kron photometry (Kron 1980) is known to capture a varying fraction of the total light, which is a function of both the Sérsic profile and S/N, e.g. the SEXTRACTOR Kron apertures capture relatively less light for galaxies with high Sérsic index or low surface brightness (see Graham & Driver 2005). In this section, we derive a correction to the SEXTRACTOR Kron magnitudes that provide a better estimate of total magnitudes.

In Figure 11 we show the difference between the SEXTRACTOR Kron magnitude and the input magnitude plotted against the SEXTRACTOR mean effective surface brightness. We have separated the comparison into four subsets based on Sérsic index and ellipticity (models FC, FE, PC, and PE as described in §4.1). The mean effective surface brightness (in units of mag arcsec^{-1}) is defined as

$$\langle \mu \rangle_e^{\text{SE}} \equiv \text{MAG_AUTO} + 1.995 + 5 \log(\text{PSCALE} \times \text{FLUX_RADIUS } 3), \quad (3)$$

where MAG_AUTO and FLUX_RADIUS_3 are the SEXTRACTOR catalog entries for Kron magnitude and the 50% light radius (in pixels), respectively, and PSCALE=0.05 arcsec pix^{-1} is the plate scale of our ACS images. We have trimmed the suite of models used in this analysis to include only those that overlap in R_{eff} - magnitude space with galaxies detected in other deep HST surveys, e.g. the Hubble Ultra Deep Field (Beckwith et al. 2006), the Groth Strip Survey (Simard et al. 2002; Vogt et al. 2005), and the Galaxy Evolution through Morphology and SEDs (GEMS; Rix et al. 2004) surveys. This was done so that corrections are estimated from models that are representative of the objects potentially detectable in our survey; the parameter space covered by these models includes the dwarf LSB galaxy population in the Coma cluster (assuming R_{eff} and magnitudes for dwarf LSBs from; Graham & Guzmán 2003).

The four panels in Figure 11 show a similar pattern, viz. photometric errors increase toward fainter surface brightness, with a systematic bias of the recovered magnitudes toward fainter values. We also note the following:

1. Despite that objects with large Sérsic indices (“P” models) have a higher detection efficiency, their SEXTRACTOR photometry have both large systematic offset in magnitude and larger scatter as compared to other models.
2. The systematic magnitude offset for models with low Sérsic index (“F” models) is relatively insensitive to surface brightness (i.e. does not exceed 0.1 mag) for models brighter than $\langle\mu\rangle_e^{\text{SE}}=23.0$.
3. The magnitudes of high-ellipticity objects (“E” models) are better recovered than the magnitudes for objects with low ellipticity (“C” models). The typical magnitude residual of a high-ellipticity model is similar to the magnitude residual of a low-ellipticity model around 0.5 mags brighter in $\langle\mu\rangle_e^{\text{SE}}$.
4. The surface brightness detection limits are the same for all four models ($\langle\mu\rangle_e^{\text{SE}}=24.75$).

In order to correct the SEXTRACTOR photometry for missing light we require the true effective radius (R_{eff}) and the Sérsic index of the galaxy (e.g. Graham & Driver 2005). The SEXTRACTOR half-light radius is a proxy for R_{eff} but is often underestimated at faint magnitudes, and also for low surface brightness objects, owing to relatively fewer pixels that satisfy the detection threshold. Instead, we derive an empirical relation between the input effective radius of our models and the output SEXTRACTOR half-light radius (`FLUX_RADIUS_3`), which is a function of the Sérsic profile, ellipticity, and $\langle\mu\rangle_e^{\text{SE}}$. This relationship is shown in Figure 12, which was fit with a fifth-order polynomial in $\langle\mu\rangle_e^{\text{SE}}$ for each of the four model groups. It is seen that the `FLUX_RADIUS_3` parameter provides a better estimate of the true R_{eff} for flat galaxy models than those with higher Sérsic indices. The best-fit conversion factor is also more or less constant for objects with low Sérsic indices that are brighter than $\langle\mu\rangle_e^{\text{SE}}=23$, while it is a steadily growing function of $\langle\mu\rangle_e^{\text{SE}}$ for high-Sérsic models. This is consistent with the systematic magnitude offsets seen in Figure 11 as described above. There are also secondary effects for the galaxy ellipticity, such that SEXTRACTOR recovers the true effective radius slightly better for low-ellipticity models. We conclude that we are able to estimate the true effective radius with good accuracy ($\sim 20\%$ rms error in the $R_{\text{eff}}/\text{FLUX_RADIUS_3}$ ratio) based on the SEXTRACTOR measurements alone, and thus perform a variable aperture correction to our catalog sources.

We have tested the reliability of performing a variable aperture correction on our suite of galaxy models. The fraction of missing light is calculated based on the ratio of the SEXTRACTOR Kron radius and the derived effective radius, and taking the known Sérsic index of the models (e.g. see Figure 9 in Graham & Driver 2005). The results are shown in Figure 13, which shows the magnitude difference between the aperture-corrected SEXTRACTOR magnitudes and the input magnitude as a function of $\langle\mu\rangle_e^{\text{SE}}$. The magnitude residuals now follow a well-defined “trumpet” diagram. Although there still exists a small systematic magnitude offset for all models at low surface brightness (especially for PE models), the magnitude offsets are not nearly as dependent on galaxy struc-

ture/shape as shown in the raw magnitude comparison in Figure 11.

We have applied this variable aperture correction to all sources in our SEXTRACTOR catalogs. We do not have prior knowledge of the Sérsic profile, thus we have performed two aperture corrections for every object using the following values for the Sérsic profile: (a) a flat profile ($n_{\text{Ser}}=1.525$) that is representative of both the majority of background galaxies and spiral/Irr galaxies inside the Coma cluster (`MAG_AUTO_CORRA`), and (b) a variable Sérsic profile given by Graham & Guzmán (2003) that scales with absolute magnitude, which is applicable to early-type galaxies in the Coma cluster (`MAG_AUTO_CORRB`); specifically, we adopt their formula $F814W=-9.4 \log n_{\text{Ser}} + 19.4$ (which assumes a color correction $F814W=B-1.3$ for early-type galaxies and a distance modulus of 35.0 mag). The photometric errors for the SEXTRACTOR corrected magnitudes are taken directly from the measured rms scatter shown in Figure 13. These errors account not only for the counting errors that are measured accurately by SEXTRACTOR but now include uncertainties related to our ability to recover the true magnitude. We have performed aperture corrections only for the F814W detections, as SEXTRACTOR apertures were not defined in the F475W band. The corrected F475W magnitude may be indirectly estimated from the SEXTRACTOR `MAG_ISO` colors and the corrected F814W magnitude, assuming a negligible color gradient outside the SEXTRACTOR aperture.

5. SUMMARY

We have improved our image pipeline based on the calibration analysis presented in this paper, and created SEXTRACTOR catalogs for 25 fields observed for the HST-ACS Coma Cluster Treasury survey. The processed images and source catalogs are publicly available for download as part of our second data release (DR2)⁴⁰. Ancillary data are also available, including the RMS and FLAG maps used as input to SEXTRACTOR, and the output SEXTRACTOR segmentation maps. The source catalogs include photometry for $\sim 76,000$ unique objects that were detected in F814W images, and color measurements for the F475W band. We performed simulations that indicate our source catalogs are 80% complete for point sources at $F814W=26.8$ mag; the simulations were also used to establish aperture corrections to the SEXTRACTOR Kron photometry. The majority of catalog sources are background galaxies, and we estimate that $\sim 5\text{--}10\%$ of objects are located inside the Coma cluster. The majority of Coma members are unresolved globular clusters, but also include a wide range of cluster member galaxies including UCDs, compact elliptical galaxies, dwarf early-type galaxies (nucleated and non-nucleated), dwarf irregular and spiral galaxies, barred disk galaxies (Marinova et al. 2010), and a cD galaxy (NGC 4874). Analysis of the observed cluster population by team members is ongoing, including but not limited to the following:

- Hoyos et al. (Paper III; 2010, *in prep*) measure the structural parameters (e.g. Sérsic index, effective radius) for $\sim 50,000$ objects selected from the Paper II photometric catalogs. Fits are performed using both GALFIT and

⁴⁰ Available at MAST (archive.stsci.edu/prepds/coma/) and Astro-WISE (www.astro-wise.org/projects/COMALS/).

GIM2D, and a detailed comparison of the useful limits for both methods is explored.

- Peng et al. (Paper IV; 2010, *submitted*) identify a large population of intracluster globular clusters (IGCs) that are not associated with individual galaxies, but fill the core of the Coma cluster and make up $\sim 40\%$ of its total GC population. The majority of IGCs are blue and metal-poor, suggesting they were ejected from the tidal disruption of dwarf galaxies, although 20% of IGCs may originate from the halos of L_* galaxies.
- Price et al. (Paper V; 2009) investigate a sample of compact galaxies that consists of old intermediate-metallicity compact elliptical (cE) galaxies, and fainter compact galaxies with properties that reside somewhere between cEs and UCDs. The measured light profiles, velocity dispersions, and stellar populations are consistent with a formation mechanism owing to tidal mass-loss from galaxy-galaxy interactions.
- Trentham et al. (Paper VI; 2010, *in prep*) measure the galaxy luminosity function (LF) to very faint magnitude ($M_{F814W}=-12$). The cluster LF is measured at different cluster-centric radii and separated by morphological class in order to study the environmental dependence of the galaxy population. Cluster membership is estimated primarily by morphology, and also using deep redshift coverage with MMT-Hectospec (Marzke et al. 2010, *in prep*) and dedicated follow-up spectroscopy with Keck-LRIS (Chiboucas et al. 2010; *submitted*).

This research and associated EPO program are supported by STScI through grants HST-GO-10861 and HST-E0-10861.35-A, respectively. Partial support is also provided for the following individuals: Carter and Karick are supported by UK STFC rolling grant PP/E001149/1; Erwin is supported by DFG Priority Programme 1177; Balcells is supported by the Science Ministry of Spain through grants AYA2006-12955 and AYA2009-11137; Hudson is supported by NSERC; Guzman is supported by Spanish MICINN under the Consolider-Ingenio 2010 Programme grant CSD2006-00070; Merritt is supported by grants AST-0807910 (NSF) and NNX07AH15G (NASA).

REFERENCES

- Beckwith, S. V. W., et al. 2006, *AJ*, 132, 1729
- Benítez, N., et al. 2004, *ApJS*, 150, 1
- Bershady, M. A., Lowenthal, J. D., & Koo, D. C. 1998, *ApJ*, 505, 50
- Bertin, E. 2006, in *Astronomical Society of the Pacific Conference Series*, Vol. 351, *Astronomical Data Analysis Software and Systems XV*, ed. C. Gabriel, C. Arviset, D. Ponz, & S. Enrique, 112
- Bertin, E., & Arnouts, S. 1996, *A&AS*, 117, 393
- Butcher, H., & Oemler, A., Jr. 1984, *ApJ*, 285, 426
- Carter, D., et al. 2008, *ApJS*, 176, 424
- Casertano, S., et al. 2000, *AJ*, 120, 2747
- Côté, P., et al. 2004, *ApJS*, 153, 223
- Cristóbal, D., Prieto, M., Balcells, M., Guzmán, R., Cardiel, N., Serrano, Á., Gallego, J., & Pelló, R. 2003, in *Revista Mexicana de Astronomía y Astrofísica Conference Series*, ed. J. M. Rodríguez Espinoza, F. Garzon Lopez, & V. Melo Martin, Vol. 16, 267
- Del Burgo, C., Carter, D., & Sikkema, G. 2008, *A&A*, 477, 105
- Dressler, A. 1980, *ApJ*, 236, 351
- Eliche-Moral, M. C., Balcells, M., Prieto, M., García-Dabó, C. E., Erwin, P., & Cristóbal-Hornillos, D. 2006, *ApJ*, 639, 644
- Ford, H. C., et al. 1998, in *Society of Photo-Optical Instrumentation Engineers (SPIE) Conference Series*, ed. P. Y. Bely & J. B. Breckinridge, Vol. 3356, 234
- Franx, M., Illingworth, G., & Heckman, T. 1989, *AJ*, 98, 538
- Fruchter, A. S., & Hook, R. N. 2002, *PASP*, 114, 144
- Graham, A. W., & Driver, S. P. 2005, *Publications of the Astronomical Society of Australia*, 22, 118
- Graham, A. W., & Guzmán, R. 2003, *AJ*, 125, 2936
- Jordán, A., et al. 2007, *ApJS*, 169, 213
- Koekemoer, A. M., Fruchter, A. S., Hook, R. N., & Hack, W. 2002, in *The 2002 HST Calibration Workshop : Hubble after the Installation of the ACS and the NICMOS Cooling System*, ed. S. Arribas, A. Koekemoer, & B. Whitmore, 337
- Komiyama, Y., et al. 2002, *ApJS*, 138, 265
- Krist, J. 1993, in *Astronomical Society of the Pacific Conference Series*, Vol. 52, *Astronomical Data Analysis Software and Systems II*, ed. R. J. Hanisch, R. J. V. Brissenden, & J. Barnes, 536
- Kron, R. G. 1980, *ApJS*, 43, 305
- Lokas, E. L., & Mamon, G. A. 2003, *MNRAS*, 343, 401
- Marinova, I., et al. 2010, *ArXiv e-prints*
- Meurer, G. R., et al. 2003, in *Society of Photo-Optical Instrumentation Engineers (SPIE) Conference Series*, ed. J. C. Blades & O. H. W. Siegmund, Vol. 4854, 507
- Peng, C. Y., Ho, L. C., Impey, C. D., & Rix, H.-W. 2002, *AJ*, 124, 266
- Pier, J. R., Munn, J. A., Hindsley, R. B., Hennessy, G. S., Kent, S. M., Lupton, R. H., & Ivezić, Z. 2003, *AJ*, 125, 1559
- Price, J., et al. 2009, *MNRAS*, 397, 1816
- Rix, H.-W., et al. 2004, *ApJS*, 152, 163
- Simard, L., et al. 2002, *ApJS*, 142, 1
- Valentijn, E. A., et al. 2007, in *Astronomical Society of the Pacific Conference Series*, Vol. 376, *Astronomical Data Analysis Software and Systems XVI*, ed. R. A. Shaw, F. Hill, & D. J. Bell, 491
- van Dokkum, P. G. 2001, *PASP*, 113, 1420
- Vogt, N. P., et al. 2005, *ApJS*, 159, 41

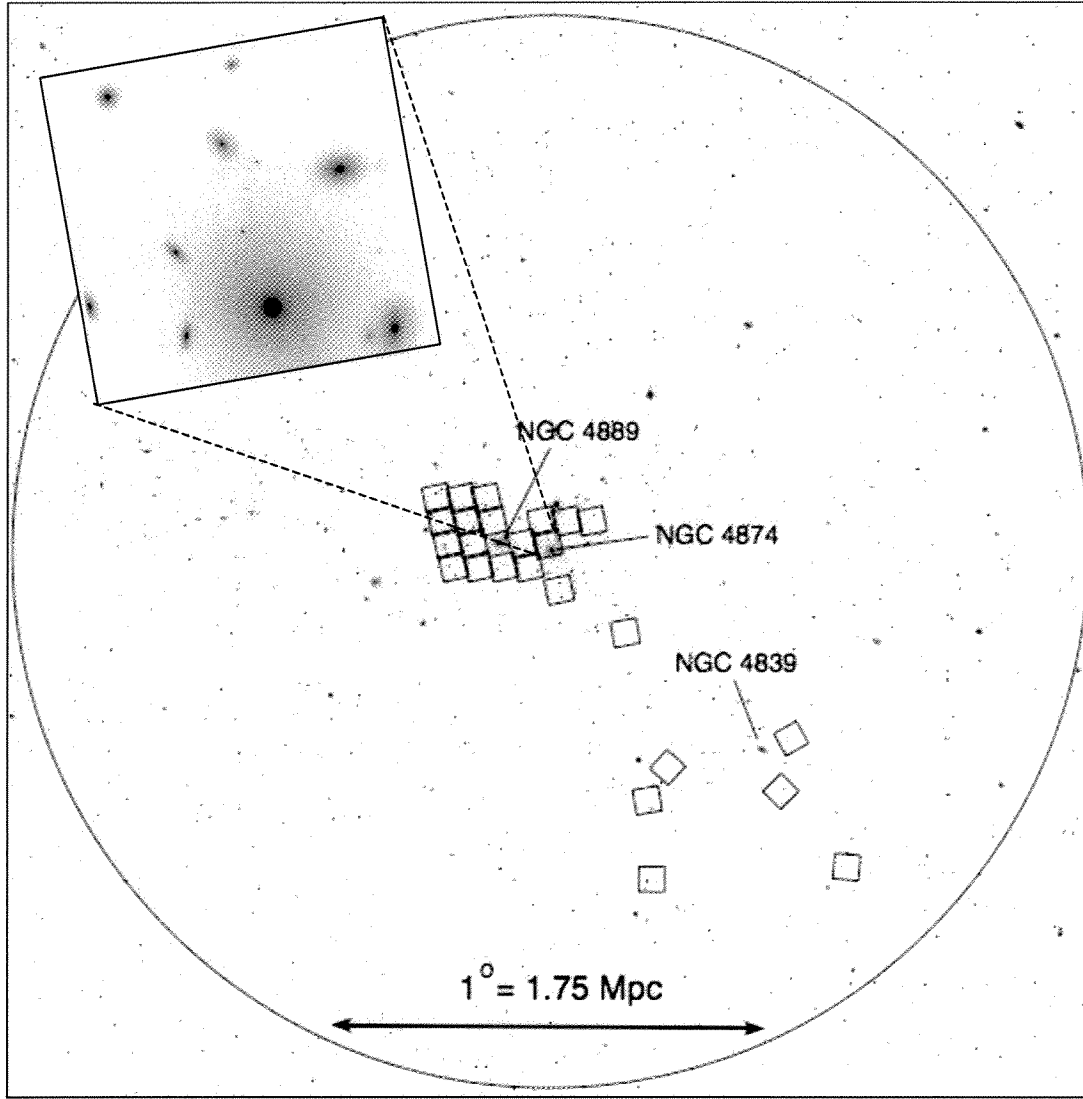


FIG. 1.— DSS image of the Coma cluster showing the location of 25 HST-ACS fields observed for the ACS Coma Treasury survey (small boxes). The large circle extends 1.24 deg from the center of the Coma cluster, or 3/4 the cluster virial radius ($r_{vir}=2.9$ Mpc; Lokas & Mamon 2003). The locations of the three largest galaxies in the Coma cluster (NGC 4889, 4874, 4839) are indicated. The inset shows the ACS image for visit-19 ($3.5' \times 3.5'$), which includes the central cD galaxy NGC 4874. North is top and East is left.

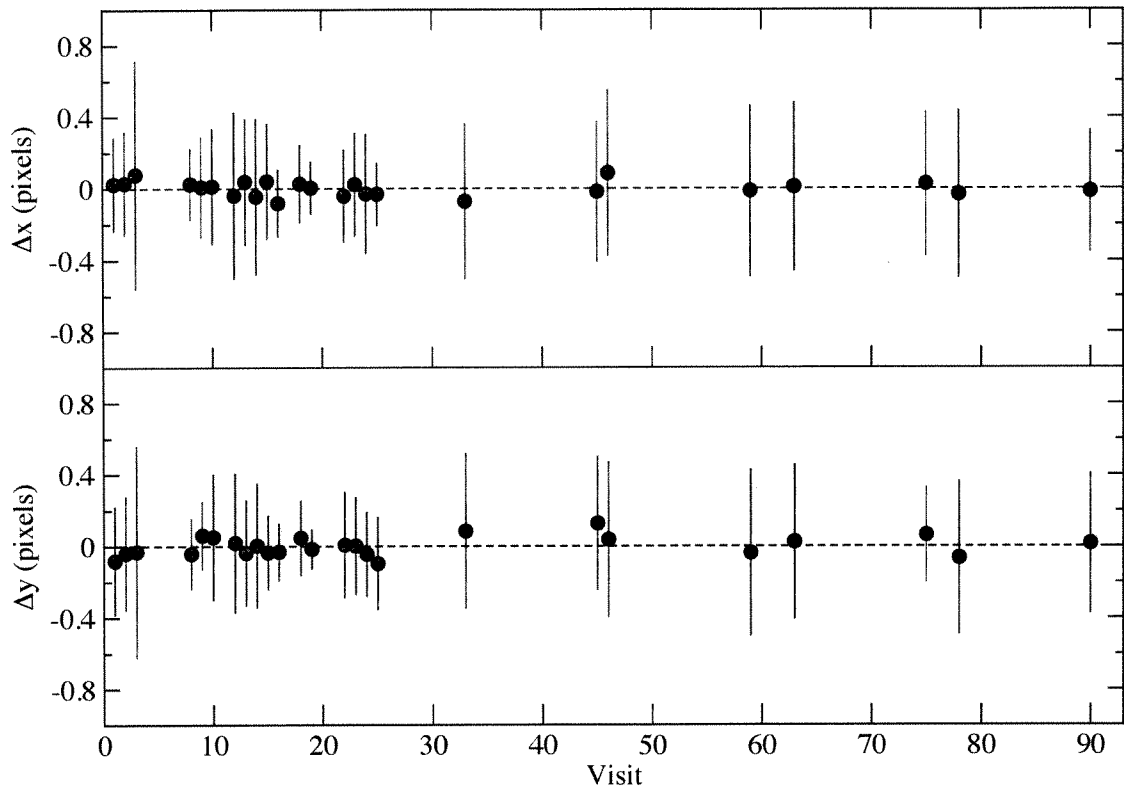


FIG. 2.— The spatial offset in pixel coordinates for identical objects detected in both the F475W and F814W images. The F475W coordinates were measured separately from the catalog presented in this study, for which we only perform source detection in the F814W band. Identical sources were selected using a 5-pixel matching radius giving 300-2000 objects for each field. Symbols indicate the 3- σ clipped average, and error bars give the 1σ rms standard deviation (not the error on the mean) for each visit. The average offset is $\lesssim 0.05$ pixels for each axis, which is a factor of six improvement over ACS images provided in the initial data release.

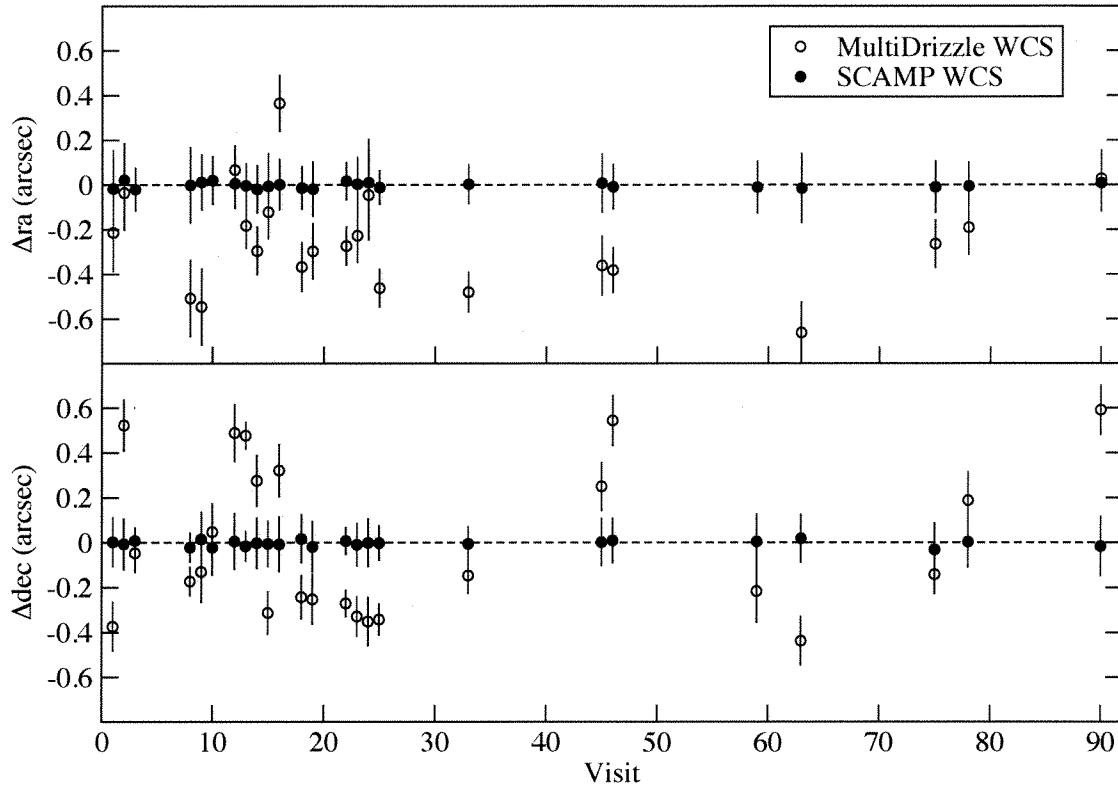


FIG. 3.— Offset in R.A. (top) and Dec. (bottom) for identical sources detected in ACS and SDSS images. The comparison was performed both before (open circles) and after (filled circles) the SCAMP software was used to align ACS images with the SDSS system. Symbols indicate the 3σ clipped average, and error bars give the 1σ rms standard deviation (not the error on the mean) for each visit. The ACS images are now aligned with the SDSS system to within $0''.04$ arcsec (i.e. the error on the mean for the total angular offset), and the 1σ rms spread in the total angular offsets is $0''.17$.

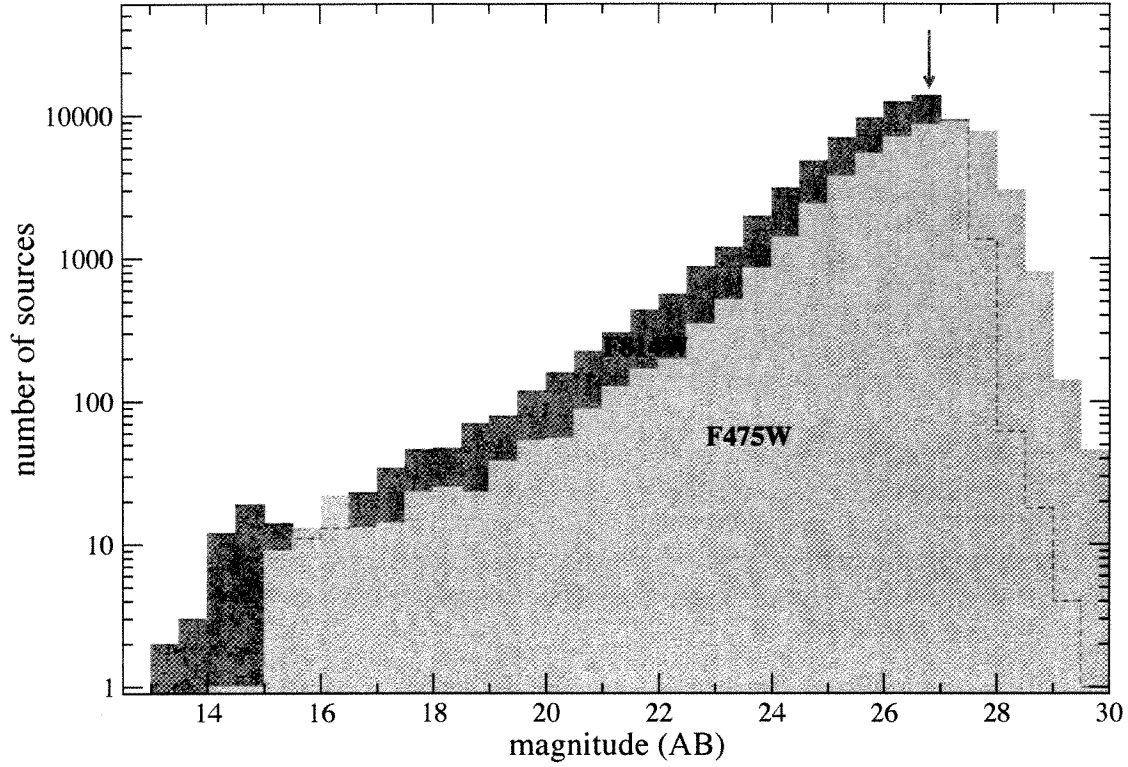


FIG. 4.— Magnitude histogram for catalog sources in both the F814W (dark shaded) and F475W (light shaded) bands. The F814W magnitudes are given for the SExtractor Kron photometry. In order to limit spurious detections, we only plot sources located in regions with full coverage by the dither pattern or bright sources ($F814W < 21$ mag). The F475W magnitudes are measured within apertures defined in the F814W image; we only show F475W sources with $S/N > 3$ to avoid including unreliable measurements. The arrow indicates the 80% completeness limit for point-sources detected in the F814W band as determined by our simulations (§4.1).

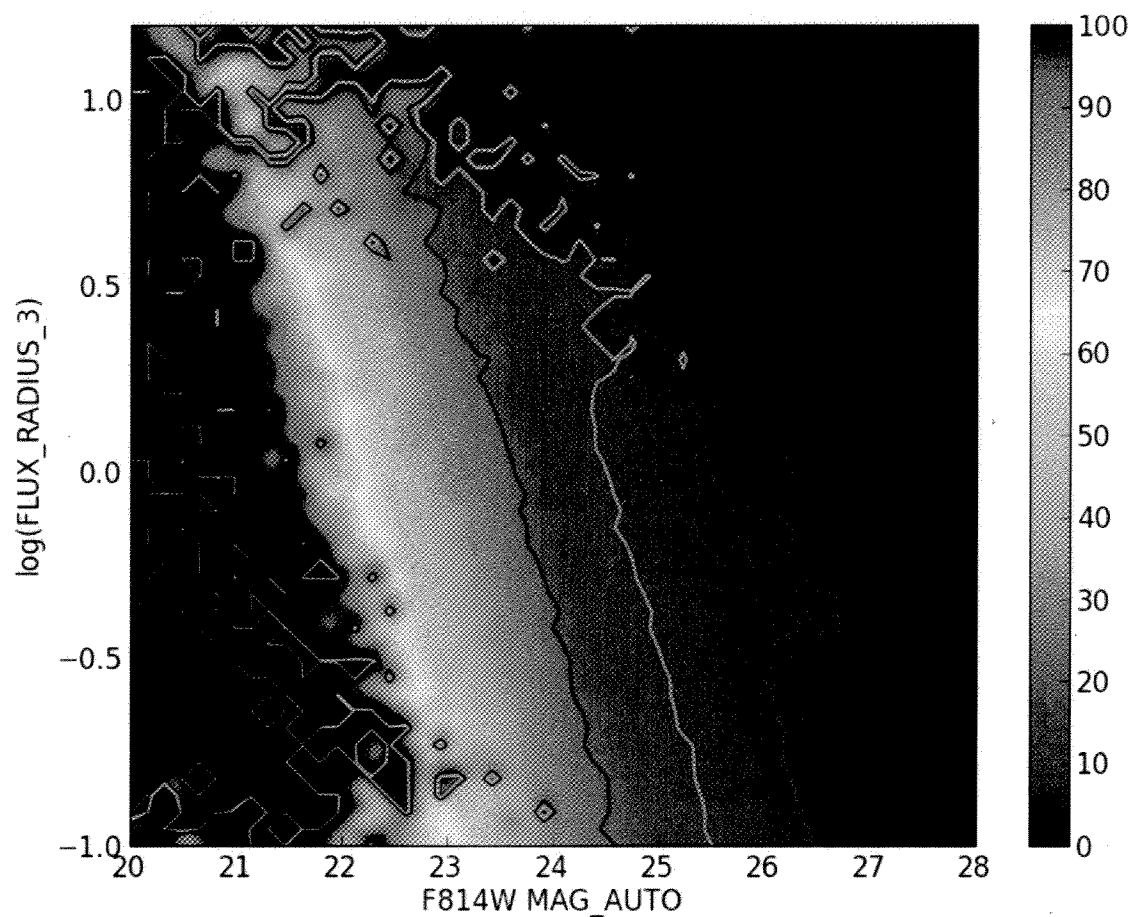


FIG. 5.— Average signal-to-noise (S/N) for catalog sources spanning the magnitude-size parameter space. Size is taken as the logarithm of the SEXTRACTOR half-light radius in arcsec, and we use the MAG_AUTO Kron magnitudes. Contours show the S/N values defined in the color bar at right. The 10σ detection limit for point sources is $F814W=26.5$ mag. The S/N is unknown in the dark blue regions located in the lower left and upper right portion of the diagram; these regions are void of source detections.

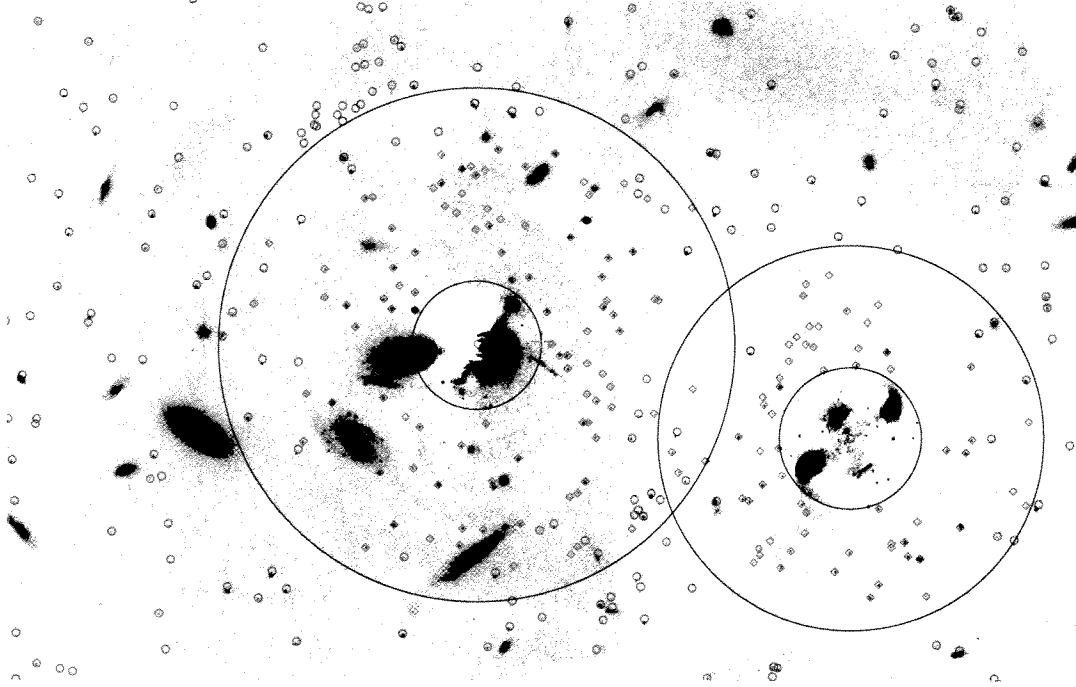


FIG. 6.— Two examples of bright galaxies that were subtracted from our images. Galaxy subtraction was performed by modeling the light distribution using the *GALPHOT* software wrapped inside Astro-WISE. Blue circles indicate sources that were detected in the original image prior to galaxy subtraction. The red circles indicate new (additional) sources that were detected after performing galaxy subtraction. The concentric circles indicate the annulus used for merging the original and new sources as described in §5; the inner/outer radius that define the annulus for each subtracted galaxy are listed in Table 3.

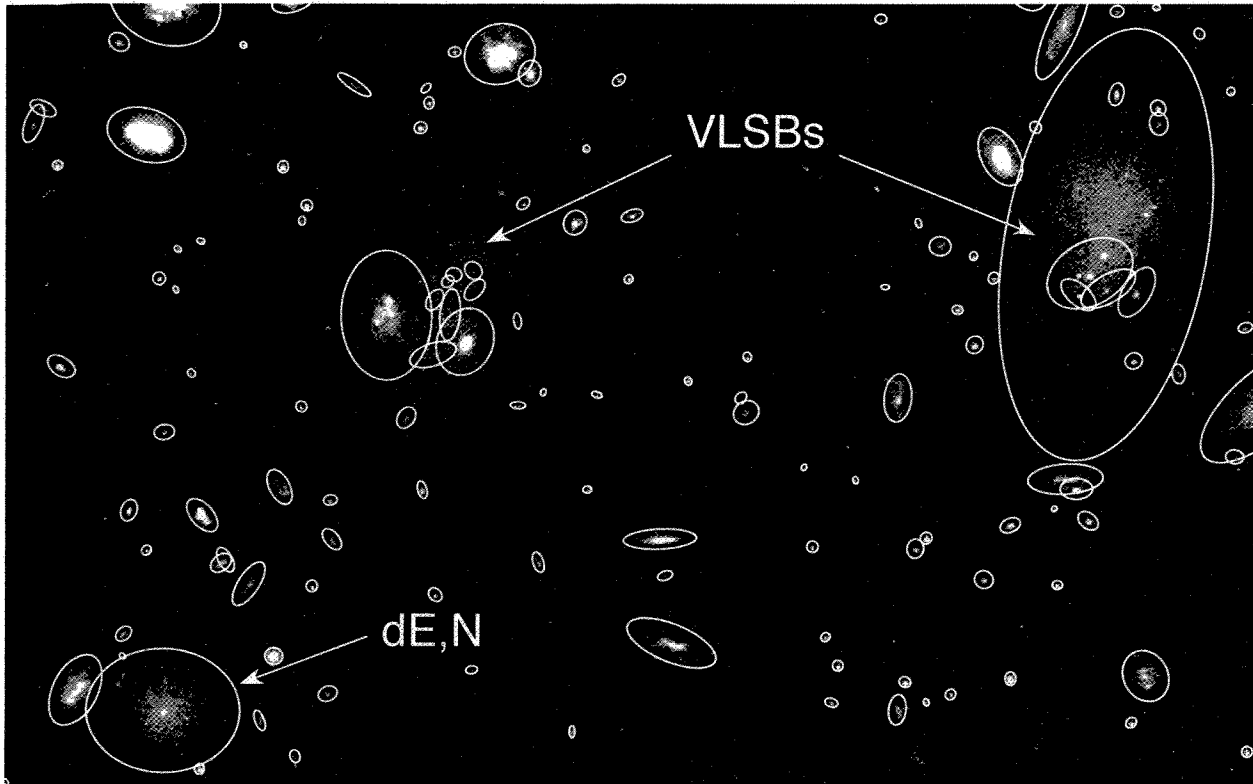


FIG. 7.— Co-added F475W and F814W image of visit-01 showing the location of two very low surface brightness (VLSB) galaxies in the Coma field. The image was binned (2x2) to improve the contrast between the VLSB galaxies and the background. The SEXTRACTOR Kron apertures (white ellipses) were measured in the F814W image. The Kron apertures for the two VLSB galaxies shown here exemplify the typical problems that we encountered: (a) galaxy shredding or a non-detection of the whole structure (VLSB galaxy located at left), or (b) poor deblending with objects located in the same light distribution (VLSB galaxy to the right). The SEXTRACTOR Kron apertures for more standard LSB dwarf galaxies in the cluster were typically well behaved (e.g. the dE,N galaxy located in the lower left of the image).

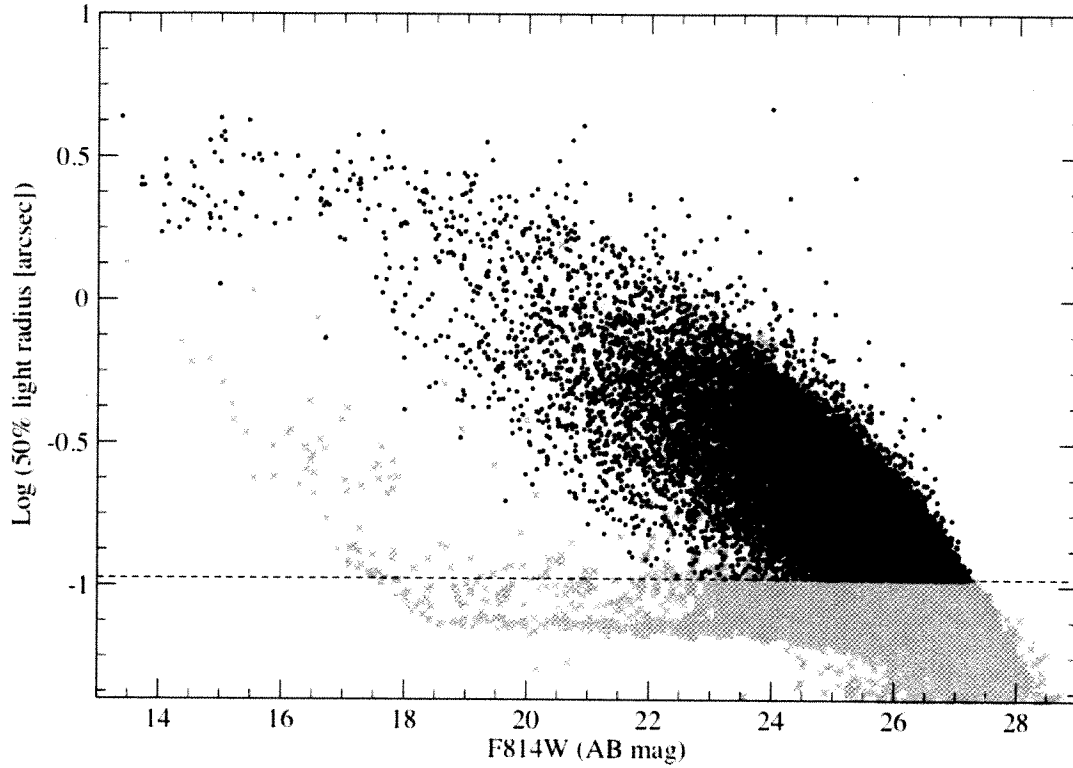


FIG. 8.— Magnitude-size diagram for catalog sources in the F814W band. Size is taken as the SExtractor half-light radius in arcsec, and we use the MAG_AUTO Kron magnitudes. In order to limit spurious detections, we only plot sources located in regions with full coverage by the dither pattern or bright sources ($F814W < 21$ mag). Gray crosses indicate point sources, and black dots show extended galaxies based on our classification scheme (§3.3.1). The dashed line is the half-light radius used to separate galaxies/point sources at $F814W > 24$ mag; both the SExtractor CLASS_STAR parameter and the half-light radius are used at brighter magnitudes. Saturated stars are responsible for the extension of point sources at bright magnitudes to larger size.

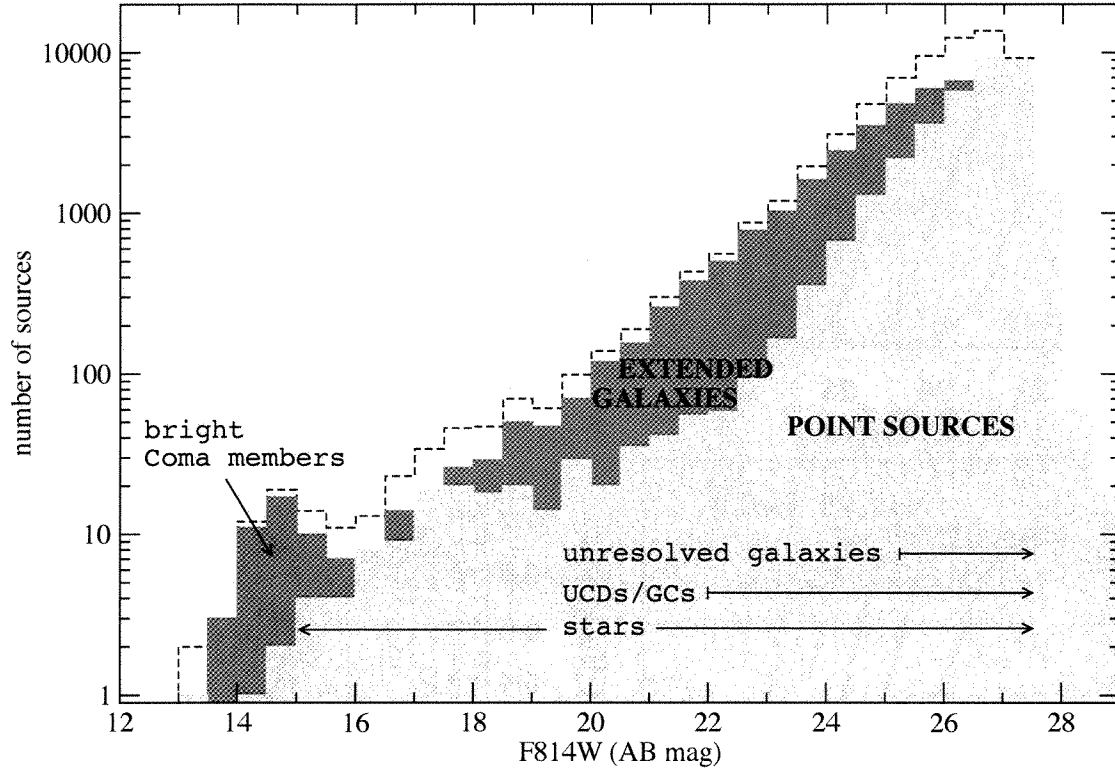


FIG. 9.— Magnitude histogram for catalog sources in the F814W band. Separate histograms are shown for objects classified as extended galaxies (dark shaded), point sources (light shaded), and the total population (dashed line). In order to limit spurious detections, we only plot sources located in regions with full coverage by the dither pattern or bright sources ($F814W < 21$ mag). For point sources, we show the magnitude range where we expect contributions from stars, UCDs/GCs, and unresolved galaxies; UCDs/GCs are likely responsible for the sharp increase in point sources at $F814=22.5$ mag. Coma members are responsible for the excess number of extended galaxies at bright magnitudes.

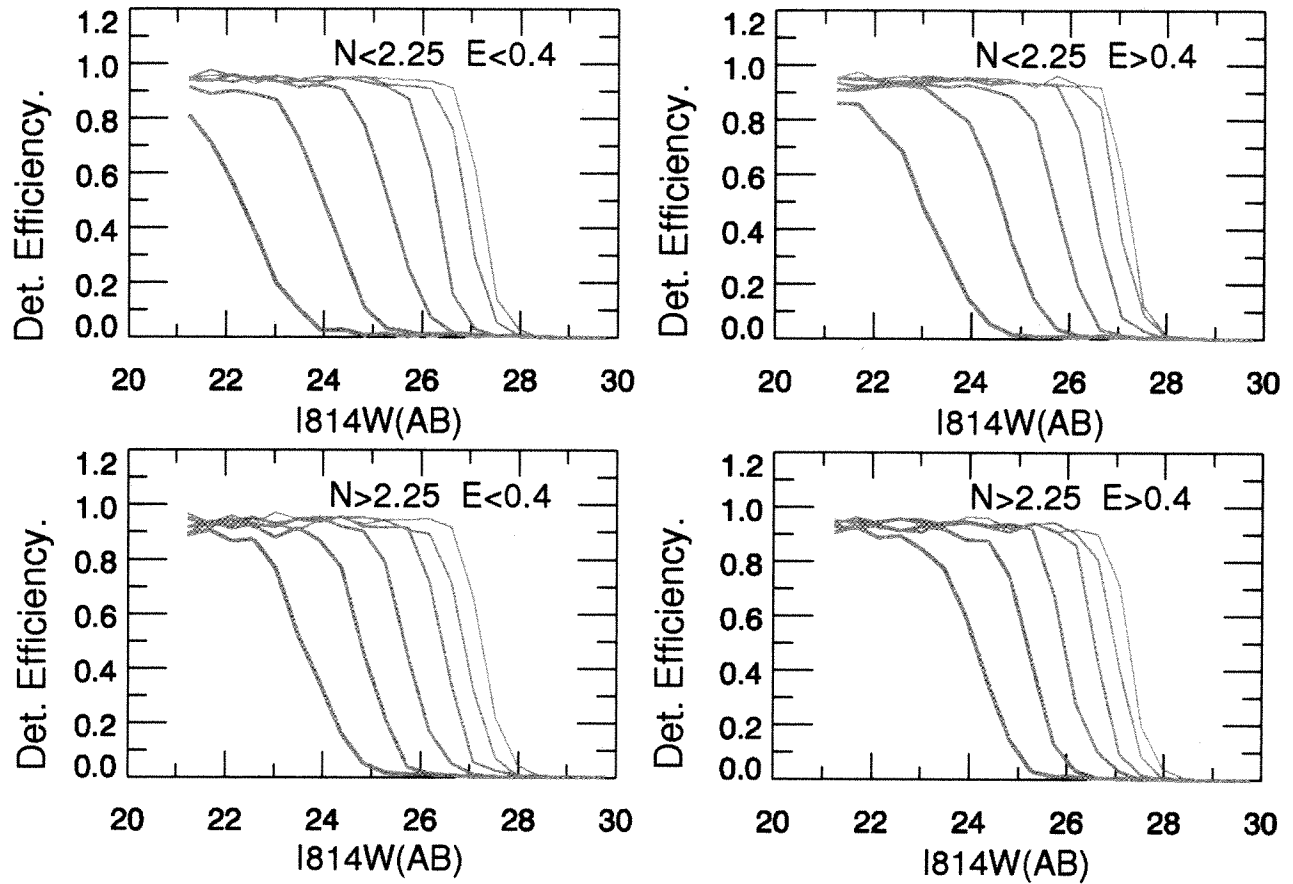


FIG. 10.— Detection efficiency curves as a function of F814W magnitude. The panels show the detection efficiency for the subset of models (FC,FE,PC,PE) that are separated by Sérsic index and ellipticity as explained in §4.1. In each panel, we further separate the models into six equally-spaced bins in logarithmic R_{eff} (the centers of the R_{eff} bins are identical to the values given in Table 2). Thin lines represent models with small R_{eff} , while thick lines are the galaxy models with large R_{eff} .

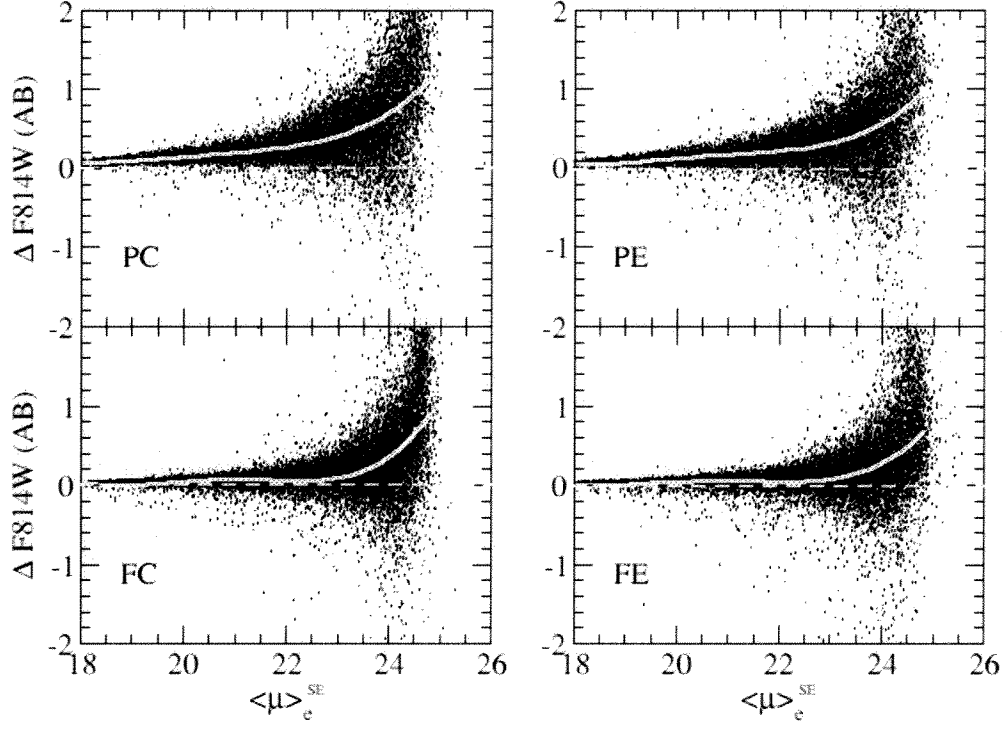


FIG. 11.— The magnitude residuals for models detected by SEXTRACTOR in the F814W band (MAG_AUTO minus input magnitude) plotted against $\langle \mu \rangle_e^{\text{SE}}$ (mag arcsec^{-2}), for models injected into the visit 1 image. The comparison is performed for the subset of models (FC,FE,PC,PE) that are separated based on Sérsic index and ellipticity as described in §4.1. The solid gray lines show the binned median offset; dashed lines show the zero magnitude offset.

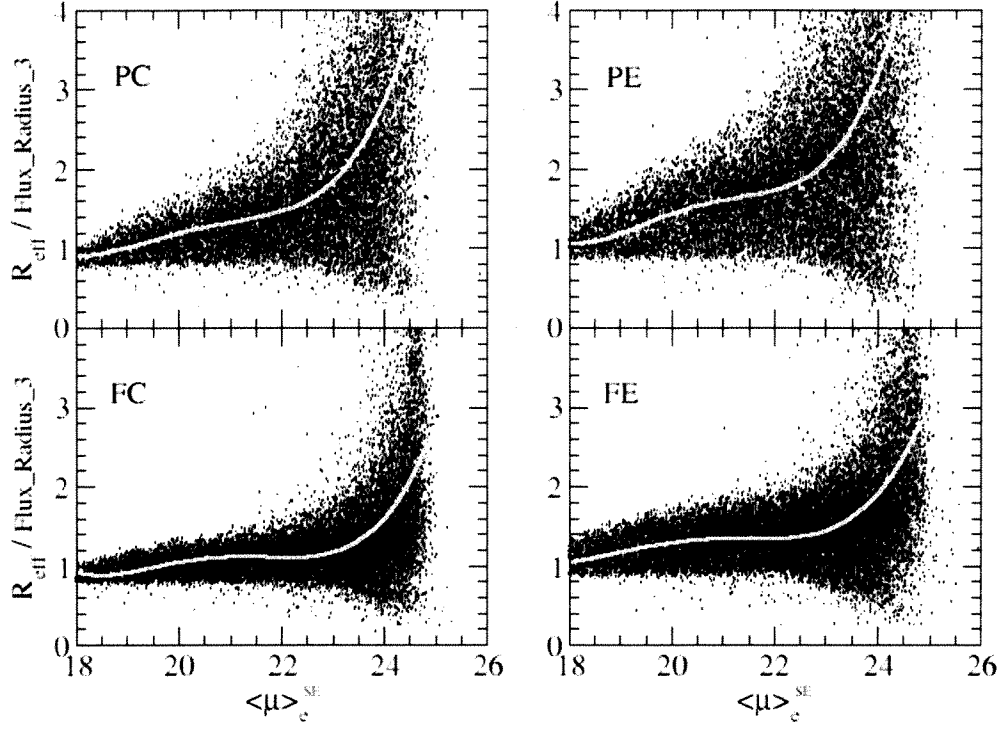


FIG. 12.— The ratio of the input effective radius and the output SETRACTOR half-light radius (FLUX_RADIUS_3) plotted against $\langle \mu \rangle_e^{\text{SE}}$ (mag arcsec^{-2}), for models injected in visit 1. The comparison is performed for the subset of models (FC,FE,PC,PE) that are separated based on Sérsic index and ellipticity as described in §4.1. Solid gray lines show 5th-order polynomial fits to the data that are used compute corrections to the Kron aperture photometry.

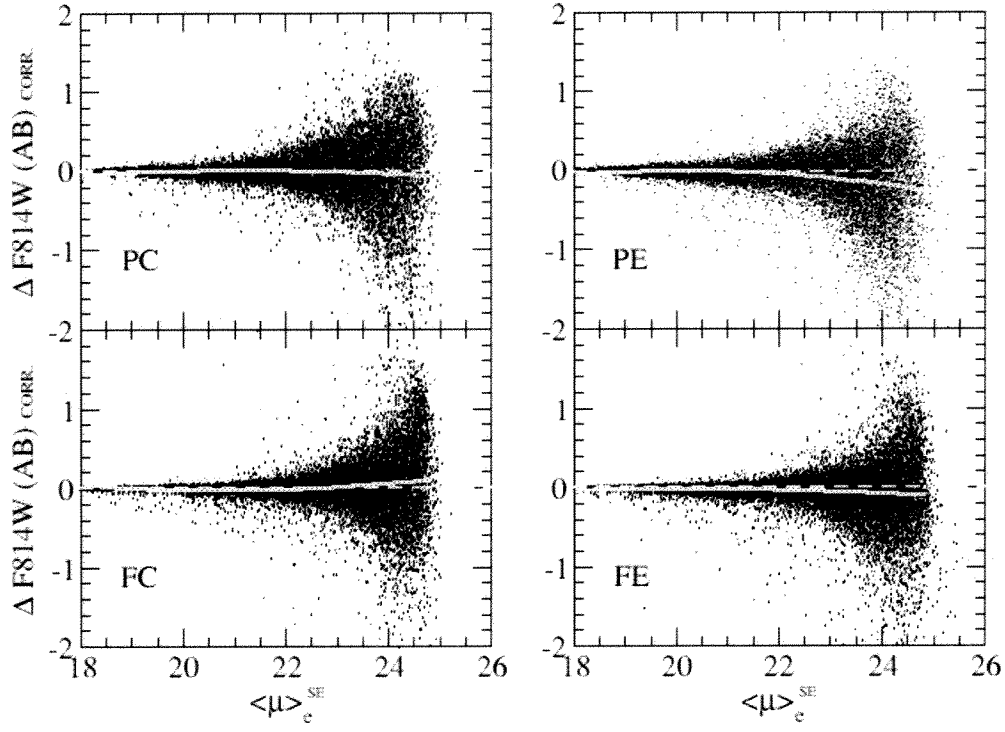


FIG. 13.— Same as Figure 11 except the magnitude residuals are plotted for the aperture-corrected SEXTRACTOR Kron photometry.

TABLE 1
FIELDS OBSERVED FOR THE HST-ACS COMA TREASURY PROGRAM

Field (visit no.) (1)	R.A. (J2000) (2)	Dec (J2000) (3)	Orient (deg) (4)	Dither Positions (5)	Exposure (sec)	
					F814W (6)	F475W (7)
01	13 00 45.90	28 04 54.0	282	4	1400	2677
02	13 00 30.30	28 04 54.0	282	4	1400	2677
03	13 00 14.70	28 04 54.0	282	2	700	1397
08	13 00 42.30	28 01 43.0	282	4	1400	2677
09	13 00 26.70	28 01 43.0	282	4	1400	2677
10	13 00 11.10	28 01 43.0	282	4	1400	2677
12	12 59 39.90	28 01 43.0	282	3	1050	2012
13	12 59 24.30	28 01 43.0	282	2	700	1372
14	12 59 08.70	28 01 43.0	282	3	1050	2037
15	13 00 38.70	27 58 32.0	282	4	1400	2677
16	13 00 23.10	27 58 32.0	282	4	1400	2677
18	12 59 51.90	27 58 32.0	282	4	1400	2677
19	12 59 36.30	27 58 32.0	282	4	1400	2677
22	13 00 35.10	27 55 21.0	282	4	1400	2560
23	13 00 19.50	27 55 21.0	282	4	1400	2677
24	13 00 03.90	27 55 21.0	282	4	1400	2560
25	12 59 48.30	27 55 21.0	282	4	1400	2560
33	12 59 29.10	27 52 10.0	282	4	1400	2677
45	12 58 21.58	27 27 40.7	318	4	1400	2677
46	12 58 34.00	27 22 58.8	280	4	1400	2677
59	12 58 31.15	27 11 58.5	270.05	4	1400	2677
63	12 56 29.80	27 13 32.8	265	4	1400	2512
75	12 58 47.75	27 46 12.7	280	4	1400	2677
78	12 57 10.80	27 24 18.0	314.52	4	1400	2677
90	12 57 04.22	27 31 34.5	299.10	4	1400	2677

TABLE 2
SIMULATED 80% COMPLETENESS LIMITS DERIVED FOR A RANGE OF STRUCTURAL PARAMETERS

Model (1)	F814W Logarithm(effective radius [arcsec])						F475W Logarithm(effective radius [arcsec])					
	Pt Src (2)	-1.08 (3)	-0.74 (4)	-0.39 (5)	-0.05 (6)	0.30 (7)	Pt Src (8)	-1.08 (9)	-0.74 (10)	-0.39 (11)	-0.05 (12)	0.30 (13)
FC	26.8	26.5	26.0	24.9	23.5	21.5	27.8	27.5	27.0	25.5	24.5	22.0
FE	26.8	26.8	26.0	25.3	24.0	22.0	27.8	27.5	27.0	26.0	25.0	23.0
PC	26.8	26.8	26.3	25.5	24.5	23.0	27.8	27.5	27.0	26.3	25.5	23.9
PE	26.8	26.8	26.1	25.5	24.7	23.5	27.8	27.7	27.2	26.5	25.5	24.5

NOTE. — F/P (flat/peak) models have Sérsic indices smaller/larger than $n_{\text{Ser}}=2.25$, and C/E (circular/elliptical) models have ellipticity smaller/larger than $e=0.4$; logarithmic effective radii are given at the center of each bin, which are equally-spaced in dex over the range $R_{\text{eff}}=0.5\text{-}60$ pixels.

TABLE 3
BRIGHT GALAXIES SUBTRACTED FROM ACS COMA IMAGES

Field (visit no.) (1)	Galaxy Name (GMP ID) (2)	R.A. (J2000) (3)	Dec (J2000) (4)	F814W Magnitude (AB)		F475W Magnitude (AB)		r_{min} (arcsec) (9)	r_{max} (arcsec) (10)
				MAG_AUTO (5)	MAG_ISO (6)	MAG_AUTO (7)	MAG_ISO (8)		
01	2440	195.20269	28.09076	13.74	13.71	15.11	15.08	7.5	20.0
03	2861	195.05360	28.07551	14.80	14.77	16.10	16.07	9.0	30.0
08	2417	195.21455	28.04300	13.70	13.66	15.08	15.03	4.0	20.0
08	2551	195.16138	28.01451	13.70	13.66	15.08	15.03	2.5	12.0
09	2727	195.09232	28.04697	14.55	14.53	15.84	15.82	4.5	15.0
10	2839	195.06144	28.04131	14.45	14.42	15.75	15.73	6.0	15.0
10	2940	195.02666	28.00441	14.98	15.02	16.26	16.31	5.3	15.0
13	3390	194.88106	28.04656	14.55	14.47	...	16.95	3.8	20.0
15	2535	195.17022	27.99663	14.56	14.53	15.87	15.85	3.0	25.0
15	2516	195.17814	27.97136	14.07	14.03	15.42	15.39	5.0	20.0
15	2510	195.17847	27.96305	14.78	14.77	16.10	16.08	5.5	15.0
16	2815	195.06884	27.96754	14.68	14.66	15.87	15.85	9.0	15.0
16	2654	195.11655	27.95599	14.83	14.81	16.14	16.12	4.5	22.0
16	2651	195.11824	27.97237	14.99	14.97	16.21	16.22	1.5	20.0
18	3170	194.94490	27.97386	14.51	14.50	15.85	15.84	4.2	25.0
19	3367	194.88662	27.98360	14.09	14.08	15.41	15.40	6.0	35.0
19	3329	194.89874	27.95927	13.38	13.36	14.76	14.74	0.0	45.0
19	3414	194.87482	27.95646	14.15	14.13	15.51	15.50	9.6	22.0
19	3213	194.93219	27.99469	14.82	14.79	16.14	16.12	3.05	20.0
22	2541	195.16564	27.92396	14.11	14.09	15.44	15.42	3.5	25.0
25	3201	194.93502	27.91248	14.10	14.08	15.40	15.38	4.5	20.0
25	3222	194.92628	27.92475	14.99	14.96	16.28	16.24	4.5	10.0
33	3423	194.87252	27.85014	14.14	14.10	15.51	15.48	8.0	25.0
33	3400	194.87844	27.88428	14.03	14.00	15.35	15.32	7.0	35.0
45	4206	194.63358	27.45635	14.91	14.89	16.19	16.17	5.5	31.0
46	4192	194.63807	27.36438	15.00	15.00	16.23	16.24	8.0	33.0
75	3958	194.71707	27.78504	14.39	14.36	15.67	15.65	5.0	34.0
78	5038	194.29486	27.40485	14.89	14.88	16.10	16.10	4.2	42.0

APPENDIX

APPENDIX A: SEXTRACTOR CONFIGURATION

We ran SExtractor in dual-image mode using the F814W band as the detection image for both filters. The SExtractor parameters used in this study are given below, including a description of the three sets of flags given for each object.

TABLE 1
PARAMETERS FOR SEXTRACTOR VERSION 2.5

Parameter	Value
ANALYSIS.THRESH	0.9
BACK_FILTERSIZE	3
BACK_SIZE	128
BACKPHOTO.THICK	64
BACKPHOTO.TYPE	LOCAL
CLEAN	Y
CLEAN.PARAM	1.0
DEBLEND.MINCONT	0.03
DEBLEND.NTHRESH	32
DETECT.MINAREA	5
DETECT.THRESH	0.9
FILTER	Y
FILTER.NAME	gauss_2.5.5x5.conv
GAIN	median exposure time (sec)
MAG.ZEROPOINT	26.068 (F475W), 25.937 (F814W)
MASK.TYPE	CORRECT
PHOT.APERTURES	2.4,8,20,30,60,90,120,180,240
PHOT.AUTOPARAMS	2.5, 3.5
PHOT.PETROPARAMS	2.0, 3.5
PHOT.FLUXFRAC	0.2,0.3,0.5,0.8,0.9
PIXEL.SCALE	0.05
SATUR.LEVEL	85,000/GAIN
SEEING.FWHM	0.12
WEIGHT.GAIN	Y
WEIGHT.TYPE	MAP_RMS, MAP_RMS
WEIGHT.THRESH	1000000, 1000000

TABLE 2
FLAGS FOR SEXTRACTOR CATALOG

Flag Value	Description
SExtractor Internal Flags (FLAGS)	
0.....	no flags
1.....	MAG_AUTO photometry may be biased by nearby neighbors (>10% of area is affected)
2.....	object was originally blended with another source
4.....	one or more pixels is saturated
8.....	object is truncated at image boundary
16.....	aperture data are incomplete or corrupted
Exposure and Image Location Flags (IMAFLAGS_ISO)	
0.....	object pixels have nominal exposure time and location
1.....	object pixel(s) are located within region of subtracted bright galaxy
2.....	object pixel(s) are located within 32 pixels of the image edge
4.....	object pixel(s) have an effective exposure less than two-thirds the nominal exposure
8.....	object pixel(s) have zero effective exposure (e.g. object is truncated by image edge)
Object Flags (FLAGS_OBJ)	
0.....	extended galaxy
1.....	point source (e.g. star, GC, UCD, or unresolved background galaxy)
2.....	cosmic ray
3.....	image artifact